ACCURACY IMPROVEMENTS FOR INTERIOR RESIDUAL STRESS MEASUREMENTS

by

XUE MEI LIU

B. Eng., Concordia University, Montreal, 1996

A THESIS SUBMITTED IN PARTIAL FULFILLMENT OF
THE REQUIREMENTS FOR THE DEGREE OF
MASTER OF APPLIED SCIENCE

in

THE FACULTY OF GRADUATE STUDIES
Department of Mechanical Engineering

We accept this thesis as conforming
to the required standard

THE UNIVERSITY OF BRITISH COLUMBIA

November, 1998

In presenting this thesis in partial fulfilment of the requirements for an advanced degree at the University of British Columbia, I agree that the Library shall make it freely available for reference and study. I further agree that permission for extensive copying of this thesis for scholarly purposes may be granted by the head of my department or by his or her representatives. It is understood that copying or publication of this thesis for financial gain shall not be allowed without my written permission.

Department of Mechanical Engineering

The University of British Columbia
Vancouver, Canada

Date Nov 9, 1998

ABSTRACT

The accuracy of interior residual stress measurements using the layer-removal, hole-drilling and ring-core methods was enhanced in two ways. In the first way, the mathematical method for calculating residual stresses from the measured strains was made more robust by applying an inverse solution method based on Linear Inverse Theory. This approach eliminates the two main weaknesses of the existing method, stress solution sensitivity to strain measurement errors and not obeying equilibrium. Optimal smoothing is introduced as an effective method for reducing sensitivity to strain data errors. With the proposed method, stress equilibrium can be easily enforced. Both experimental and theoretical results show that the inverse solution method stabilizes the calculation procedure and it is an effective and reliable method for determining residual stresses in a material.

The second way of enhancing residual stress measurement is to develop a new residual stress measurement technique. The new technique, called ring-hole drilling, overcomes the limitations of strain sensitivity to subsurface stresses of the hole-drilling and ring-core methods. By moving the strain gauges from the material surface to the interior, the overall strain sensitivity of the ring-hole drilling method is increased to double that of the ring-core method, and about four times that of the hole-drilling method. The experimental measurements made with ring-hole method correspond very closely with theoretical expectations determined using finite element method. The results show that ring-hole drilling is a practical method for evaluating residual stresses in a material.

TABLE OF CONTENTS

LIST OF FIGURES

LIST OF TABLES

NOMENCLATURE

σ_θ = circumferential stress in a cylinder

σ_a = axial stress in a cylinder

E = modulus of elasticity

ν = Poisson's ratio

$\varepsilon_\theta^{"}$ = circumferential strain reliefs

$\varepsilon_a^{"}$ = axial strain reliefs

$\Psi(r)$ = combination of circumferential and axial strain reliefs

$\Lambda(r)$ = combination of circumferential and axial strain reliefs

r = inner cylinder radius

r_a = initial inside radius of a cylinder

r_b = outer cylinder radius

R = general radius for evaluating the integral

j = index for each data point

d_j = jth datum

g_j = jth kernel function

m = unknown model function

$\| m \|^2$ = model norm

α_j = expansion coefficients

Γ = n x m matrix

d_j^{pro} = produced jth datum

χ^2 = statistical variable

s_j = standard deviations

Φ = objective function to be minimized

μ = Lagrange multiplier

s_d = diagonal matrix

P_j = power series function

l_j = piecewise linear function

A, B = calibration coefficients for infinitesimal relieved strains

$\overline{A}$, $\overline{B}$ = calibration coefficients for strain guage area relieved strains

$\overline{a}$, $\overline{b}$ = normalized form of the calibration coefficients $\overline{A}$, $\overline{B}$

σ_{max} = maximum principal residual stress

σ_{min} = minimum principal residual stress

ε_r = radial strain reliefs

ε = relieved strain measured by the strain gauge rosette

ε_h = average strain over the strain gauge grid area corresponding to the applied hydrostatic stress

ε_s = average strain over the strain gauge grid area corresponding to the applied shear stress

ε_1 = strains measured by the strain gauge 1

ε_2 = strains measured by the strain gauge 2

ε_3 = strains measured by the strain gauge 3

γ = angular coordinate of the radial mid axis of the strain gauge measured counterclockwise from the maximum principal stress

β = angle measured clockwise from gauge 3 to the maximum principal stress direction

r = generalized hole radius

r_a = straight hole radius

r_m = strain gauge main radius

h = hole depth

ACKNOWLEDGMENT

I would like to thank my supervisor, Dr. Gary Schajer, for providing me with this research opportunity, as well as his invaluable guidance, encouragement, care and attention throughout the study.

I appreciate the financial support made by the Natural Science and Engineering Research Council of Canada (NSERC).

My appreciation also goes to Dr. Douglas Oldenburg for his guidance on solving inverse problems, and to Len Drakes and Tony Basic for machining and supervising me in machining the experimental equipment.

Finally, I would like to express my gratitude to my family and my friends who have enthusiastically supported my studies, especially my husband Xiaozhong Li and son Terry for their love, care and support, my friends Margaret and Ted Kass and Ted's sister Raye kass for their encouragement, care and support.

1. INTRODUCTION

1.1 Residual Stresses

Residual stresses are locked-in stresses, which exist in a material without the presence of any external load. They are commonly induced by manufacturing processes that involve non-uniform plastic deformation, for example, rolling, drawing, extrution and bending. Residual stresses can also be produced by the non-uniform dimensional changes involved in processes such as welding and casting. Subsequent installation and assembly procedures can also be a source of residual stresses, for instance by tightening bolts or by press fitting components [1].

Residual stresses profoundly affect material performance. Tensile residual stresses are generally detrimental and can greatly accelerate material failure due to fatigue and stress corrosion. They can cause significant dimensional change when stressed material is added or removed. Conversely, compressive residual stresses are generally beneficial and are often induced deliberately [2]. For example, metal components are often shot-peened to increase their fatigue life. Also, glass is often 'tempered' to increase its working strength.

Due to their significant effects, residual stresses must be taken into account in engineering design. A good understanding of residual stress in a material can reduce the need for excessive safety factors, and promote economical and safe design. Accurate residual stress measurement is therefore a basic requirement.

Conventional methods for measuring stresses due to applied loads are not suitable for measuring residual stresses. In typical methods, the applied stresses are evaluated indirectly by comparing the current strain state with the zero strain state (by removing or applying external loads). However, there are no external loads in the case of residual stresses. Thus, specialized stress measurement methods are needed.

1.2 Residual Stress Measurement Methods

Many different methods for measuring residual stresses have been developed in the past. They can be divided into two main categories:

1. non-destructive methods
2. destructive methods.

1.2.1 Non-Destructive Methods

The main non-destructive methods for measuring residual stresses are X-ray, neutron diffraction and ultrasonic. These methods are attractive because they do not cause any damage to the specimen. They therefore can be used for production quality control. However, the required equipment is costly, especially in the case of neutron diffraction, where a nuclear reactor is needed. The measurement accuracy is also fairly modest.

The X-ray method [3] uses an X-ray beam to irradiate a metal so that the distance between the crystallographic planes can be measured. This distance is changed by the state of

stress of the material. Since the X-ray can only penetrate a few micrometers into a metallic material, the X-ray method is limited to measuring surface stresses. It is often used to estimate a material fatigue life and crack propagation.

Based on an analogous principle, the neutron diffraction method [4] transmits neutrons throughout the thickness of the metal material. Unlike the X-ray method, which can only measure surface residual stresses, neutron diffraction can determine residual stresses throughout the thickness. However, due to the weak sources of neutrons, this method has modest accuracy. In addition, the method has restricted practical application because it requires the availability of a nuclear reactor. The measurement cost is correspondingly high.

The ultrasonic method [5] is based on the small dependence of sonic wave speed on the residual stresses in a material. The change in wave speed is proportional to the average residual stress. Since the ultrasonic method measures only the average stress, significant stress gradients cannot be identified.

1.2.2 Destructive Methods

The most common destructive techniques for measuring residual stresses are the layer-removal method, the hole-drilling method and the ring-core method. These methods are based on the fact that removal of stressed material disturbs the stress equilibrium, resulting in measurable deformations in the remaining material. These methods have the advantages of low cost and greater accuracy compared with non-destructive methods. The disadvantage is

the damage to the specimen. As a result, destructive methods are suitable only for mass production or where loss of the specimen can be tolerated.

The layer-removal method [6] is a well-established technique for measuring residual stresses in planar or cylindrical components. In this method, one or more strain gages are used to measure the strain changes caused by the removal of successive layers of stressed material from elsewhere in the specimen. The original residual stresses existing in a specimen can then be calculated from the measured strains. In planar specimens, the layers can be removed as shown in figure 1.1.(a). In cylindrical specimens, the layers can be removed as shown in figure 1.1.(b). Typically, layer removal involves almost complete destruction of the specimen.

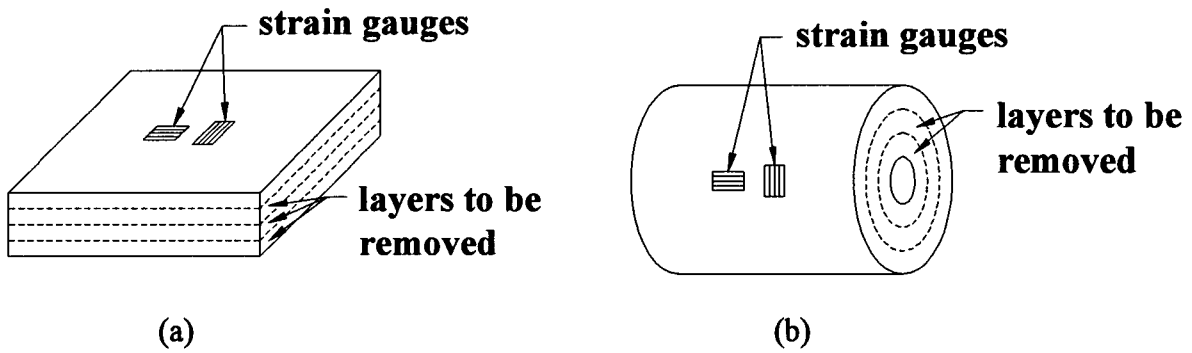

Fig 1.1 Layer-Removal Method.

Layer-removal involves almost complete strain relief, and is potentially the most accurate method of all destructive methods for measuring residual stresses. However, a weakness of this method is that the equations for calculating the subsurface stress distribution contain differential quantities and the evaluation of these quantities creates calculation errors due to noise contained in the strain data. The method is also quite time-consuming.

The hole-drilling and ring-core methods are the most common destructive methods for measuring residual stresses. Both involve local removal of stressed material and measurement of the strain relief in the adjacent material surface. Since the removal of the material is relatively small and often tolerable, these methods are sometimes described as 'semi-destructive'.

The hole-drilling method [7] involves drilling a small hole, typically 0.040-0.200 inches (1-4 mm) in diameter and depth, and measuring the surface strains around the hole by using a specially designed strain gage rosette (see figure 1.2 (a)). The original residual stresses can then be calculated from the measured strains. This method is limited by its sensitivity since only about 25 percent of the strain is relieved by drilling a hole. Thus, great care must be taken with the measurements to achieve an acceptable accuracy.

Another method similar to hole-drilling is the ring-core method [7]. In this method, a 0.600-6.000 inches (15-150 mm) diameter ring core is machined (see figure 1.2 (b)), and the relieved strain on the surface of the material remaining inside the ring is measured.

The ring-core method is more sensitive than the hole-drilling method because it involves almost complete strain relief. The disadvantage of the ring-core method is that the size of the ring is relatively large. It causes much more damage than the hole-drilling method.

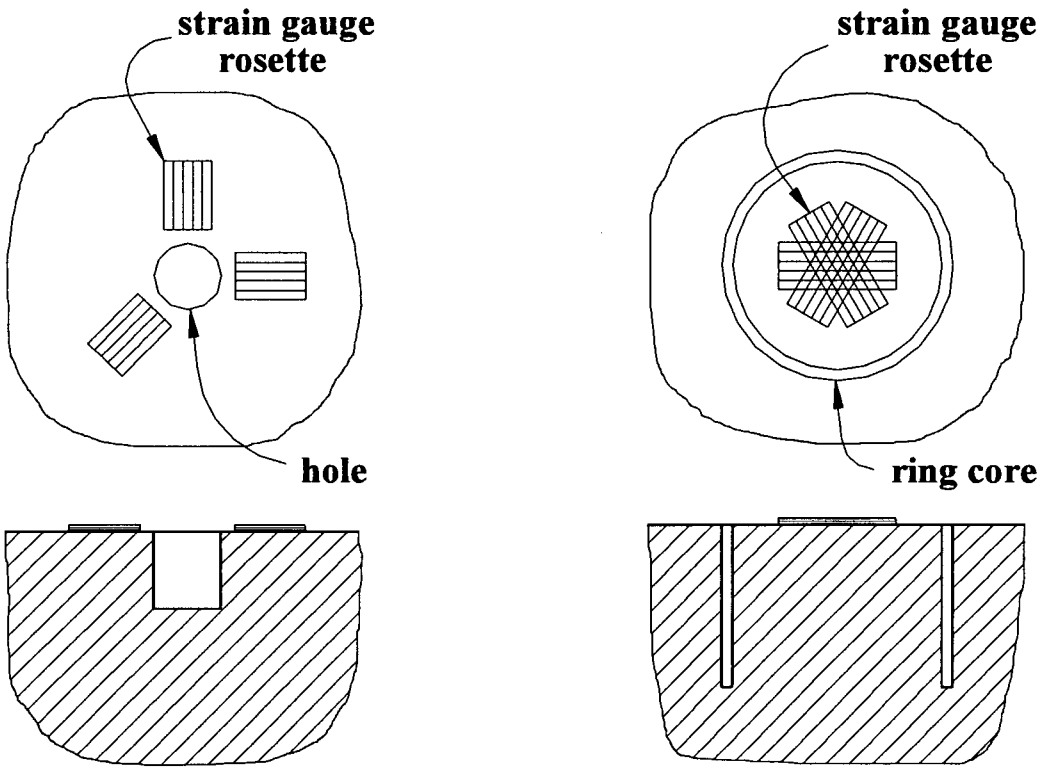

a. Hole-Drilling Method

b. Ring-Core Method

Fig 1.2 Hole-Drilling and Ring-Core Methods.

Despite their simplicity and popularity, both the hole-drilling and the ring-core methods are relatively insensitive to the stress variations in the interior. This occurs because the strain gauges are placed on the material surface, far away from the location of the interior stresses. In recent years, there has been growing interest in identifying the details of the subsurface stresses. This study focuses on ways of improving the interior stress evaluation capabilities of destructive residual stress measurement methods such as layer removal, hole-drilling and ring-core.

1.3 Previous Work

The discussion here focuses on the three most common destructive methods the layer-removal method, the hole-drilling method and the ring-core method. These three methods form the basis of all the research work presented in this thesis.

1.3.1 Layer-Removal Method

As shown in figure 1, the layer-removal method can be used with either planar or cylindrical specimens. The most common application is for cylindrical specimens, and is known as Sachs' boring-out method. In 1927, Sachs introduced thick cylinder theory to relate the residual stress in each removed layer to the change diameter of the remaining part. In this theory, the relationship between the residual stresses originally present in the cylinder and the measured strains is expressed in terms of a differential equation, referred to as Sachs' equation [8]:

$$\sigma_\theta(r) = \frac{E}{1-\nu^2}\left(\frac{r_b^2 - r^2}{2r}\frac{d\Psi(r)}{dr} - \frac{r_b^2 + r^2}{2r^2}\Psi(r)\right) \qquad (1.1)$$

where $\sigma_\theta(r)$ is the circumferetial stresses in a cylinder, E is the modulus of elasticity, ν is Poisson's ratio, r_b is the outer radius of the cylinder and $\Psi(r) = \varepsilon\theta'' + \nu\varepsilon_a''(r)$ is a combination of the circumferential and axial strain relieves measured at the outside surface when the boring-out has reached an inner radius r. However, numerical evaluation of the differential quantity $\frac{d\Psi}{dr}$ is an inherently unstable process, and so the accuracy of the stress calculation is significantly compromised. Also, the differential solution method does not ensure that stress equilibrium is obeyed.

In 1953, Lambert [9] expressed residual stresses in a cylinder in terms of an integral equation. He described a solution method in terms of Legendre polynomials which was too computationally intensive for routine work at that time. Also, the published method is slightly in error because the Legendre polynomials do not retain their orthogonality properties after layers have been removed.

Dodd [10] experimentally verified Sachs' boring-out method. In his experiment, Dodd bored out a cylinder in seven steps and measured the strain changes on the outside surface of the cylinder. He also calculated the original residual stresses by using Sachs' method. In addition, he pointed out that Sachs' method fails to ensure stress equilibrium.

In 1989, Hung [11] developed a data-acquisition system which greatly accelerated Sachs' boring-out method. By using the system, he was able to obtain the stress profile in a cylinder within few hours. However, the equations that Hung used to calculate residual stresses were Sachs' differential equations, and so his calculations were still sensitive to strain measurement errors and do not necessarily obey equilibrium.

1.3.2 Hole-Drilling Method

The hole-drilling method was first introduced by Mathar in 1932. He used a mechanical extensometer to measure the displacements around a circular through-hole in a thin plate [12]. In 1950, Soete and Vancrombrugge replaced the mechanical extensometer with electrical strain gages, and improved the ease of measurement and the accuracy of the method [13].

In 1956, Kelsey [14] described a procedure for using the hole drilling method to measure non-uniform residual stresses. In his research work, instead of using through holes he used blind holes which eliminated the limitations of the method to thin plates. In 1966, Rendler and Vigness developed a standardized rosette [15]. Through their work, the hole drilling method became a systematic and easily reproducible procedure. The ASTM E837 standardized hole drilling rosette was typically defined.

The theoretical development of the hole drilling method continued. In 1978, Bijak-

Zochowski [16] identified that the increment of the strains on the surface not only depends on the stresses that exists in the increment depth but also depend on the geometry changes due to the deepening of the hole.

In 1981, Schajer [17] provided the first generalized finite element analysis of the hole drilling method, including tabulations of all calibration coefficients. Continued in 1988, he published a detailed investigation on using the hole-drilling method for determining residual stress variation with depth, and provided the required finite element calibrations [18].

1.3.3 Ring-Core Method

In parallel with the development of the hole-drilling method, the ring-core method was introduced by Milbradt [19] in 1950 as a more sensitive alternative to the hole-drilling method. In his investigation, an annular ring was milled concentrically around a wire resistance gauge which was mounted within the ring. An additional small central hole was made to guide the tool for cutting the ring. Milbradt compared the ring-core and the hole-drilling methods, and concluded that the ring-core method involves almost full stress relaxation while the hole-drilling method only involves about 25 percent stress relaxation.

Gunnert [20] advanced the ring-core method by using foil strain gauge rosettes. Wolf and Böhm later used a small end mill mounted eccentrically in a cutting head to machine the annular ring. They also determined the minimum needed depth of the ring to achieve 100 percent stress relaxation [21]. Continued, in 1988, Böhm, Stücker and Wolf introduced a

standardized strain gauge rosette termed a ring-core rosette [22]. Since then, the ring-core method was open to wider application. However, because of the greater amount of machining involved, the ring-core method is less popular than the hole drilling method.

1.4 Objectives and Overview

The objective of this research is to improve the interior stress evaluation capabilities of layer removal, hole-drilling and ring-core methods. The work follows two main approaches, improved mathematical methods for computing residual stresses from the measured strains, and improved methods for making strain measurements that are more sensitive to the interior stresses.

Currently, two problems exist in the layer-removal method. First, the calculations of the method is based on solving Sachs' differential equations, which is a process sensitive to strain measurement errors. Second, the method does not guarantee that stress equilibrium is obeyed. A different calculation approach is developed in the first part of this study to eliminate these problems.

The approach taken is to reformulate Sachs' differential equation (equation 1.1) into the form of an integral equation. This change avoids the problem of having to evaluate the strain derivatives and allows other mathematical solution methods to be used. An inverse solution method based on Linear Inverse Theory [23] is used to solve the integral equation. The advantages of this method is that it provides a more stable procedure for evaluating the

integral equation. Also, stress equilibrium is easily enforced. The first part of this thesis describes and explains the application of the inverse solution method and examines different integral solution results as well as comparing them with Sachs's results.

A new residual stress measurement technique, Ring-Hole Drilling, is introduced in the second part of this study to improve the sensitivity of the measured strains to the interior stresses. The new method combines aspects of both the hole-drilling and ring-core methods. It involves drilling a central hole and then a surrounding annular ring. The new method overcomes the interior stress resolution limitations of the previous two methods by moving the strain gauges from the specimen surface into the central hole. In this way, the relieved strains are measured in an area much closer to the location of the desired interior stresses. Measurement sensitivity and stress resolution are thereby greatly increased.

The second part of this thesis describes the proposed ring-hole method in detail. The sensitivity of the new method is compared with that the hole-drilling and the ring-core methods. Experimental measurement of the strain sensitivity of the method is compared with numerical results.

2. IMPROVED LAYER-REMOVAL CALCULATION METHOD

This chapter describes the physics and governing equations for typical layer-removal methods. It goes on to develop some mathematical techniques that are effective in solving the governing equations. The objectives of these techniques are to achieve as realistic as possible residual stress solutions that are stable in the presence of measurement errors, and to enforce stress equilibrium.

2.1 Layer-Removal Method

The layer-removal method is a widely used method for measuring residual stresses in planar or cylindrical components. In this method, one or more strain gauges are attached to a material surface. They are used to measure the strain changes caused by the removal of successive layers of stressed material from elsewhere in the specimen. The original residual stresses existing in the specimen can then be calculated from the measured strains.

Figure 2.1.(a) shows the application of the layer removal method to a planar specimen. The strain gauges are attached on the top surface and the material is removed layer by layer from the bottom surface. Figure 2.2.(b) shows the application of the layer removal method for a cylindrical specimen. The strain gauges are placed on the outer surface of the cylinder and the material is removed from the inside. Alternatively, the strain gauges can be placed on the inside surface and the material removed from the outside.

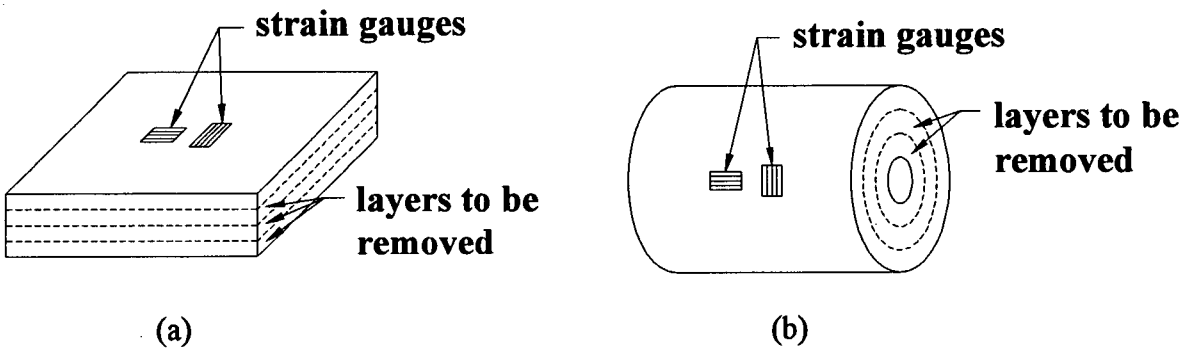

(a) (b)

Fig 2.1 Layer-Removal Method.

Since the removal of the material covers the entire surface, the various layer-removal methods involve almost complete strain relief. They are the most accurate and the most destructive of the various methods for determining interior residual stresses.

2.1.1 Differential Equation Solution

The Sachs' boring-out method [8] is the most commonly used layer removal method. It involves successive cutting out of layers of material from the interior of a cylindrical specimen, and measuring the resulting strain changes on the outside surface using strain gauges. Removal of each interior layer releases the residual stresses that were contained in that layer and redistributes them throughout the remaining material. The relieved circumferential and axial strains are measured after each bore by the strain gauges. Differential equations based on thick cylinder theory, called Sachs' equations [8], are then used to determine the original residual stresses that were contained in the cylinder. The

equations for calculating circumferential and axial stresses in a cylinder from the measured strains as the cylinder is bored-out from the interior are:

$$\sigma_\theta(r) = \frac{E}{1-\nu^2}\left(\frac{r_b^2 - r^2}{2r}\frac{d\Psi(r)}{dr} - \frac{r_b^2 + r^2}{2r^2}\Psi(r)\right) \tag{2.1}$$

$$\sigma_a(r) = \frac{E}{1-\nu^2}\left(\frac{r_b^2 - r^2}{2r}\frac{d\Lambda(r)}{dr} - \Lambda(r)\right) \tag{2.2}$$

where,

$$\Psi(r) = \varepsilon_\theta^*(r) + \nu\varepsilon_a^*(r) \tag{2.3}$$

$$\Lambda(r) = \nu\varepsilon_\theta^*(r) + \varepsilon_a^*(r) \tag{2.4}$$

$\sigma_\theta(r)$ and $\sigma_a(r)$, are respectively the circumferential and axial stresses at radius r. E is modulus of elasticity , ν is the Poisson's ratio and r_b is the outer radius of the cylinder. $\Psi(r)$ and $\Lambda(r)$ are strain quantities combining the circumferential and axial strain reliefs measured at the outside surface when the boring-out has reached an inner radius r.

Two problems exist when determining residual stresses using equations 2.1 and 2.2. The first is that equations 2.1 and 2.2 can be evaluated only if $\frac{d\Psi}{dr}$ and $\frac{d\Lambda}{dr}$ are determined. This is done either numerically or graphically. However, $\Psi(r)$ and $\Lambda(r)$ are measured only at a discrete set of cylinder radii r, corresponding to the sequence of radii in the boring out operation. Then $\frac{d\Psi}{dr}$ and $\frac{d\Lambda}{dr}$ can only be approximately determined. This approximation is

very prone to errors. Moreover, when the strain measurements contain experimental errors, the estimation of $\frac{d\Psi}{dr}$ and $\frac{d\Lambda}{dr}$ will be further degraded. The combination of insufficient and erroneous strain measurements yields poor estimates for $\frac{d\Psi}{dr}$ and $\frac{d\Lambda}{dr}$. Thus, the accuracy of the calculations of σ_θ and σ_a are therefore significantly compromised [23].

The second problem in the solution method is that it does not ensure that stress equilibrium is obeyed. In order to be in equilibrium, the following conditions must be enforced:

$$\int_{r_a}^{r_b} \sigma_\theta \, dr = 0 \tag{2.5}$$

$$\int_{r_a}^{r_b} \sigma_a \, r \, dr = 0 \tag{2.6}$$

Equation 2.6 can be transformed into the format of equation 2.5 using the enclosed area $A = \pi r^2$ as the independent variable. With this change in variable, equation 2.6 becomes:

$$\int_{A_a}^{A_b} \sigma_a \, dA = 0 \tag{2.7}$$

Conformity to equilibrium equations 2.5 and 2.6 is not guaranteed in the presence of measurement and discretization errors.

2.1.2 Integral Equation Solution

An alternative approach can be taken that largely overcomes the shortcomings of using equations 2.1 and 2.2 for evaluating residual stresses. Integration of equations 2.1 and 2.2 gives [9]:

$$\frac{E}{1-\nu^2}\ \Psi(r) = \frac{-2r}{r_b^2 - r^2} \int_r^{r_b} \sigma_\theta(R)\ dR \tag{2.8}$$

$$\frac{E}{1-\nu^2}\ \Lambda(r) = \frac{-2}{r_b^2 - r^2} \int_r^{r_b} \sigma_a(R)\ R\ dR \tag{2.9}$$

where, R is the general radius used for evaluating the integral. These are Volterra equations of the first kind. Notice that, equations 2.8 and 2.9 can also be derived from stress equilibrium (see appendix).

In most integral equations, the unknown terms are on the left side and the known terms appear within the integrals on the right. Such problems are called forward problems and can be solved by direct integration. However, in equations 2.8 and 2.9, the known quantities $\Psi(r)$ and $\Lambda(r)$ appear on the left, while the unknown stress functions $\sigma_\theta(R)$ and $\sigma_a(R)$ are inside the integrals on the right. This feature significantly complicates the solutions of equations 2.8 and 2.9 since they cannot be simply integrated. Such equations are called inverse problems. Linear Inverse Theory can be used to solve inverse problems of the type of equations 2.8 and 2.9.

2.2 Linear Inverse Theory

Linear Inverse Theory is a set of mathematical techniques to extract information about physical properties of objects or systems from experimental observations that appear in integrated form [24]. Usually, the observations consist of tabulations of measurements, or "Data". The results are numerical values representing the physical or statistical properties of the problem. These properties are called model parameters. The relationship between the model parameter and the data is called the Model. A model can be based on physical or statistical relationships. For example, to determine the density of the liquid contained in a bottle based on the measurements of the mass and the volume of the liquid [24], there are two Data, mass d_m and volume d_v and one unknown model parameter, density m_1. The statement that density times volume equal mass will be the Model and can be written in vector form as $d_v m_1 = d_m$.

Considering equations 2.8 and 2.9, the Data are the strain measurements $\Psi(r)$ and $\Lambda(r)$ and the Models are the stress distributions $\sigma_\theta(R)$ and $\sigma_a(R)$. Since equations 2.8 and 2.9 are linear inverse problems, linear inverse theory is a suitable method for solving these equations. The advantage of using this method is that the model construction process allows the incorporation of constraints that the model has to satisfy such as the stress equilibrium condition. More importantly, the constructed model is fairly stable with respect to data errors.

The primary goal of solving an inverse problem is to construct a model from the observed data. Most experiments can provide only a limited amount of discrete data while most models are continuous. Therefore, a nonuniqueness exists, so that many models may fit the same set of data. However, most of these models are unrealistic. They typically contain results that oscillate around a central trend. A unique model with minimal oscillations can be achieved by requiring that the model norm is minimized. The norm is the mathematical abstraction of the length of a vector. When applying experimental data, a weighted norm can be used to accommodate different types of data with different measurement accuracies. The general procedures for obtaining a minimum norm model solution from both accurate and inaccurate data are explained in this chapter.

2.2.1 Minimum Model Norm Solution from Accurate Data

When constructing a model from accurate data, equation 2.8 and 2.9 can be written in general form as [23]:

$$d_j = (g_j, m) = \int_0^a g_j(x)\ m(x)\ dx \qquad (2.10)$$

$$j = 1,2,3, \cdots N.$$

Equation 2.10 is a Fredholm equation of the first kind, where, d_j is the jth datum, g_j is the jth kernel function, (g_j, m) is the inner product (or the generalization of the dot product), m is the unknown model function and x is an independent variable. For example, in the case of

equation 2.8, d represents the measured strain quantity $\frac{E}{1-\nu^2}\Psi(r)$, m represents the stress σ_θ, g corresponds to the factor $\frac{-2r}{r_b^2 - r^2}$ and x corresponds to radius r. Notice that g_j is assumed known or can be determined from physical knowledge of the problem. In this case, g_j is assumed to be a set of linearly independent elements.

Construction of a Model with a minimum model norm from accurate data involves minimization of the model norm ($\| m \|^2$) subject to the data constraint. The minimization can be achieved in practice by assuming that the model can be expressed as a linear combination of the kernel functions [25]:

$$m = \sum_{j=1}^{N} \alpha_j g_j \tag{2.11}$$

where α_j are the unknown expansion coefficients to be determined. Substitute m into equation 2.10:

$$(g_j, \sum_j \alpha_j g_j) = d_j \qquad j = 1,2,3,\cdots N. \tag{2.12}$$

or written as:

$$\sum_{j=1}^{N} (g_i, g_j)\, \alpha_j = d_j \qquad i = 1,2,3,\cdots N. \tag{2.13}$$

This system of equations can be written in matrix form:

$$\Gamma \alpha = d \tag{2.14}$$

where $$\Gamma_{ij} = (g_i, g_j) = \int_0^a g_i(x)\, g_j(x)\, dx \tag{2.15}$$

Since Γ is a symmetric and positive definite matrix, Γ^{-1} therefore exists, and α can be determined as:

$$\alpha = \Gamma^{-1} d \tag{2.16}$$

Since α_j and g_j are known quantities, the model with minimum model norm from accurate data can now be recovered from equation 2.11.

2.2.2 Minimum Model Norm Solution from Inaccurate Data

Most experimental data are contaminated with errors. Therefore, when attempting to construct a realistic model, it is desirable that the model should concentrate on the underlying physical information, and try to ignore data errors. This means that the data to which the model corresponds, called the produced data, are not exactly the same as the experimental data. The difference between the produced data and the experimental is called the misfit. Typically, the produced data can be considered as a "smoothed" form of the experimental data. The objective is that the produced data should contain much smaller errors than the original experimental data.

The data errors are not individually known. However, it can be assumed that they are independent variables, with a normal distribution, zero mean and standard deviations s_j. With such errors, an appropriate value for the misfit is given by the chi-squared statistic [23]:

$$\chi^2 = \sum_{j=1}^{N} \frac{(d_j - d_j^{pro})^2}{s_j^2} \tag{2.17}$$

where, d_j is the observed datum, d_j^{pro} is the produced datum by the model and s_j is the standard deviation of jth datum and is used to normalize the data. χ^2 is a statistical variable whose expected value is approximately equal to N the number of data for $N \geq 5$. If $\chi^2 << N$, the data are over fitted. The models have more structure than the true model and these structures are artifacts of the noise contained in the data. Conversely, if $\chi^2 >> N$, the data are poorly fitted. The information contained in the data about the model is lost. The models display less structure than the true model. Consequently, the optimum model should satisfy the requirement that the model reproduces the data with χ^2 misfit close to N.

A model from inaccurate data can be constructed by minimizing the model norm subject to the misfit criterion. The objective function to be minimized is expressed by Φ as [25]:

$$\Phi = \|m\|^2 + \mu \left(\sum_{j=1}^{N} \left(\frac{d_j - d_j^{pro}}{s_j} \right)^2 - N \right) \tag{2.18}$$

where, μ is the Lagrange multiplier which trades off between the model norm and the misfit criterion. From equations 2.10, 2.11. 2.12. 2.13. 2.14 and 2.15, the model norm $\|m\|^2$ and data d_j^{pro} can be written in matrix form:

$$\|m\|^2 = (m, m) = \left(\sum_{j=1}^{N} \alpha_j g_j , \sum_{j=1}^{N} \alpha_j g_j \right) = \alpha^T \Gamma \alpha \qquad (2.19)$$

$$d_j^{pro} = (g_j , m) = \left(g_j , \sum_{j=1}^{N} \alpha_j g_j \right) = \Gamma \alpha \qquad (2.20)$$

where, α^T is α transpose. Therefore, equation 2.18 also can be written in a matrix form:

$$\Phi = \alpha^T \Gamma \alpha + \mu \left(\| s_d (d - \Gamma \alpha) \|^2 - N \right) \qquad (2.21)$$

where, s_d is a diagonal matrix whose elements are $(s_d)_{jj} = \frac{1}{s_j}$. When minimizing equation 2.21 with respect to parameters α and μ, a system of equations is obtained as:

$$\left(\Gamma + \frac{1}{\mu} S \right) \alpha = d \qquad (2.22)$$

and

$$\chi^2 = N \qquad (2.23)$$

where S is also a diagonal matrix whose elements are $S_{jj} = s_j^2$. This matrix augments the Γ matrix. Equation 2.26 can be solved iteratively by finding the value of the Lagrange multiplier μ that gives the required misfit $\chi^2 = N$ and the corresponding α. The model from inaccurate data can then be recovered in the same way as before from equation 2.11.

Equation 2.22 is very similar to equation 2.14 for the case where model fits the experimental data exactly. The data misfit is associated with the term $\frac{1}{\mu}S$. In general, all experimental data are contaminated with error, and so equation 2.26 is a more appropriate choice than equation 2.14. Use of equation 2.22 requires an estimate of the standard deviation of the measurement errors, s_j. In the limiting case where $s_j \rightarrow 0$, there is no data misfit, and equation 2.22 becomes the same as equation 2.14. As the standard deviation of the measurement error increases, the data misfit and the associated data smoothing increases. The $\chi^2 = N$ criterion provides a convenient method for identifying the optimal smoothing required.

2.2.3 Using Different Functions

With a different approach, the stresses in equation 2.10 can be expressed as a linear combination of the other functions such as polynomials or piecewise linear functions. For example, when using polynomials, the kernel functions in equation 2.11 will be replaced by the polynomials. When fitting data exactly, the procedures listed in equations 2.11 to 2.18 is unchanged. However, the Γ matrix will be formulated by the kernels and the polynomials:

$$\Gamma_{jk} = \left(g_j, p_k\right) = \int_0^a g_j(x)\ p_k(x)\ dx \tag{2.24}$$

In this case, Γ is typically not symmetric. If requiring misfitting the data, replace kernel function g_j with polynomials p_j in equations 2.19, 2.20 and 2.21. The smoothing equation 2.22 then becomes:

$$\left(\Gamma + \frac{1}{\mu} S\left(\Gamma^T\right)^{-1} P\right) \alpha = d \tag{2.25}$$

where,
$$P_{jk} = \left(p_j, p_k\right) = \int_0^a p_j(x)\ p_k(x)\ dx \tag{2.26}$$

Equation 2.25 corresponds to equation 2.22, and becomes exactly the same if $p_j(x) = g_j(x)$. It can be solved in the same way by iteratively finding the value of the Lagrange multiplier μ that gives the optimum misfit and the corresponding α.

In the following chapter, practical examples of the use of equation 2.14, 2.22 and 2.25 are presented for solving the integral equation 2.8 and 2.9 governing residual stress measurements by the layer removal method. The characteristic features of some particular choices of the functions in equation 2.11 will be explored.

3. INVERSE SOLUTIONS

This chapter describes a procedure for solving integral equations 2.8 and 2.9 using Linear Inverse Theory. Several important practical characteristics of the solution are explored. They include:

1. how well the solution determines the stress results when the given strain data are "exact".
2. how stable the solution is in the presence of strain measurement errors.
3. how smoothing can be used to reduce sensitivity to strain data errors.
4. how much the stress results are distorted by the use of smoothing.

To explore these characteristics effectively, it is convenient to use synthetic data rather than measured data. The synthetic data are created by starting with an assumed stress distribution and then using equations 2.8 and 2.9 in a forward calculation to determine the corresponding strains. These strains are then used as the basis for an inverse calculation to determine the associated stresses. Finally, the effectiveness of the inverse calculation is assessed by comparing how well the calculated stresses reproduce the original assumed stresses.

In this chapter, synthetic data are used to explore the above four characteristics of the proposed linear inverse calculations. Several variations of these calculations are presented,

each with slightly different computational features. An application to practical laboratory data is also discussed.

3.1 Solving Integral Equations from Synthetic Data

Most experimental measurements contain unknown errors. When determining stresses from experimental strain readings, it is difficult to test the stability of the solution since the data errors are not known. To simplify the process, a set of synthetic data is generated and applied. The synthetic data used here are based on the experimental results of Dodd [10]. He measured the strain changes on the outside surface of a solid aluminum alloy cylindrical specimen, 1.5 inches in radius, caused by successive boring out of material from the central part of the cylinder. The cylinder was bored successively 7 times at the radii r = [0.455, 0.65, 0.85, 1.05, 1.15, 1.25, 1.35] inches. Seven sets of strain readings corresponding to the cylinder radii for circumferential and axial strains were measured.

The synthetic data are generated by choosing a function as a stress distribution:

$$\sigma_\theta(r) = 1 - \frac{2r}{r_b} \tag{3.1}$$

and integrating it through the domain. This function provides a straight line which has the property of zero integral over the cross-section. Equilibrium is therefore obeyed.

Based on the number of experimental data points, 7 synthetic data were created corresponding to the radii of the boring operation done by Dodd. An extra datum $d_j = 0$ and

kernel function $g_j = 1$ was obtained from the equilibrium equation 2.5. In this way, the set of 8 data listed in table 3.1 was generated.

Table 3.1 Synthetic Data

Radius of Bored Out Cross Section (inches)	Synthetic Strain Data (d_j)
0	0
0.455	-0.14119352
0.65	-0.26201550
0.85	-0.40992908
1.05	-0.57647059
1.15	-0.66540881
1.25	-0.75757576
1.35	-0.85263158

3.1.1 Solution Using Kernel Functions

Equation 2.8 is first solved by assuming that the stress is a linear combination of the kernel functions. The first step is to reformulate equation 2.8 to a standard inverse integral form as equation 2.10. To achieve this, a Heaviside Unit Step function is introduced to the kernel functions. The standard inverse form is written as:

$$d_j(r) = \int_0^{r_b} g_j(r)\ m(r)\ dr \qquad (3.2)$$

where, j is the index corresponding to each cylinder radius at the point of boring, $d_j(r)$ is the jth strain datum, $g_j(r)$ is the corresponding kernel functions and m(r) is the circumferential stress model to be determined. These parameters correspond to:

$$d_j(r) = \frac{E}{1-\nu^2}\,\Psi(r) \tag{3.3}$$

$$g_j(r) = \frac{2\,r_j}{r_b^2 - r_j^2}\,H(r-r_j) \tag{3.4}$$

$$m(r) = \sigma_\theta(r) \tag{3.5}$$

Notice that a Heaviside Unit Step function is contained in each kernel function. Therefore, the kernels are step functions as shown in figure 3.1

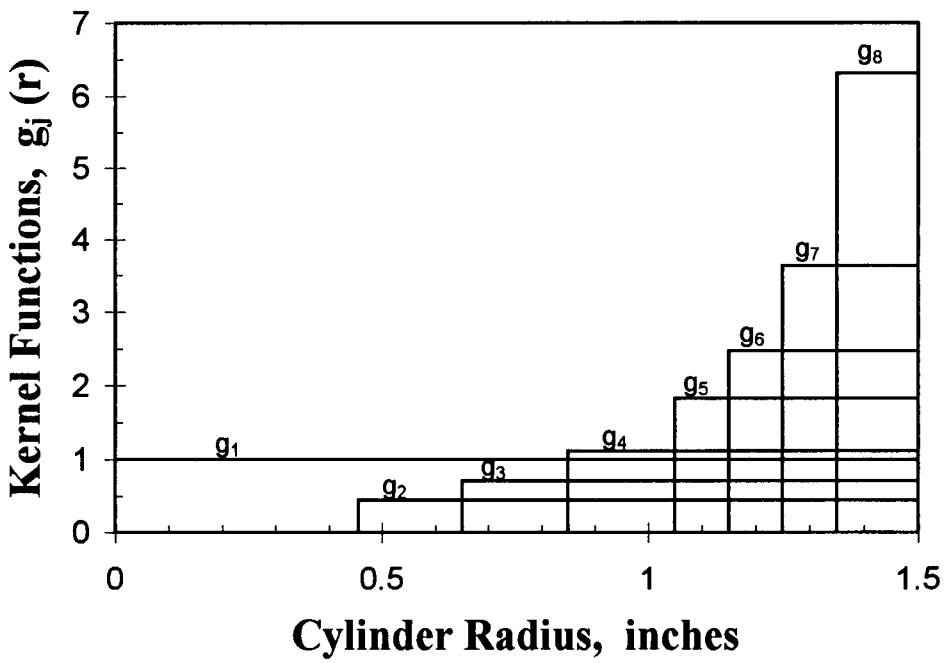

Figure 3.1 Kernel Functions.

For the case where the strain data are exactly fitted, equation 2.16 is used to obtain the coefficients α_j. Following the steps that listed in chapter 2 from equation 2.11 to 2.16, a minimum norm solution (see figure 3.2) is obtained.

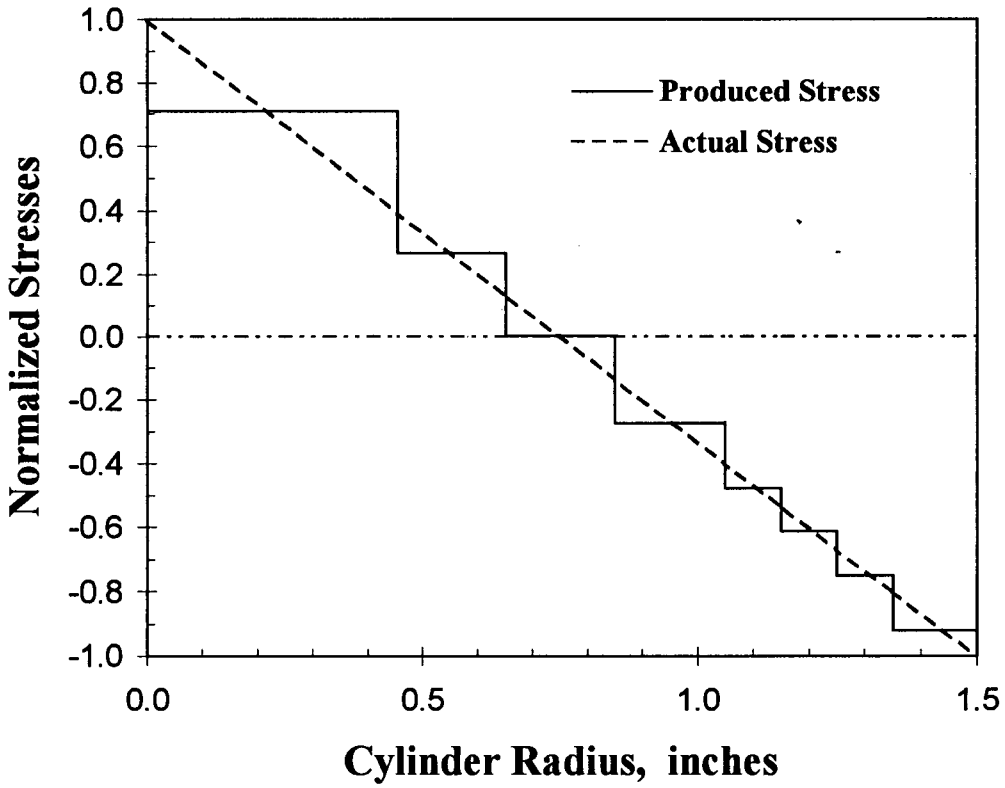

Figure 3.2 Stresses from Kernel Functions with No Smoothing and No Data Errors.

Figure 3.2 shows a plot of the stress profile produced by the kernel function solution. The model originally used to generate the synthetic data, labeled Actual Stress, is also plotted. It can be seen that the produced stress oscillates about the actual stress. The staircase shape is caused by the assumption that the stress profile is a linear combination of the

step kernels. In figure 3.2, equilibrium is obeyed because the stress profile possesses a zero integral across the cylinder radius.

The effect of strain measurement error was simulated by corrupting the strain data by adding random errors to each of the seven non-zero strains in Table 1. These data errors were randomly selected to be in the range of ± 1 % of the maximum strain data. Ten such data sets were produced. Notice that the resulting relative errors in the early strain data is much greater than ± 1 % because these strain data are much smaller than the maximum strains.

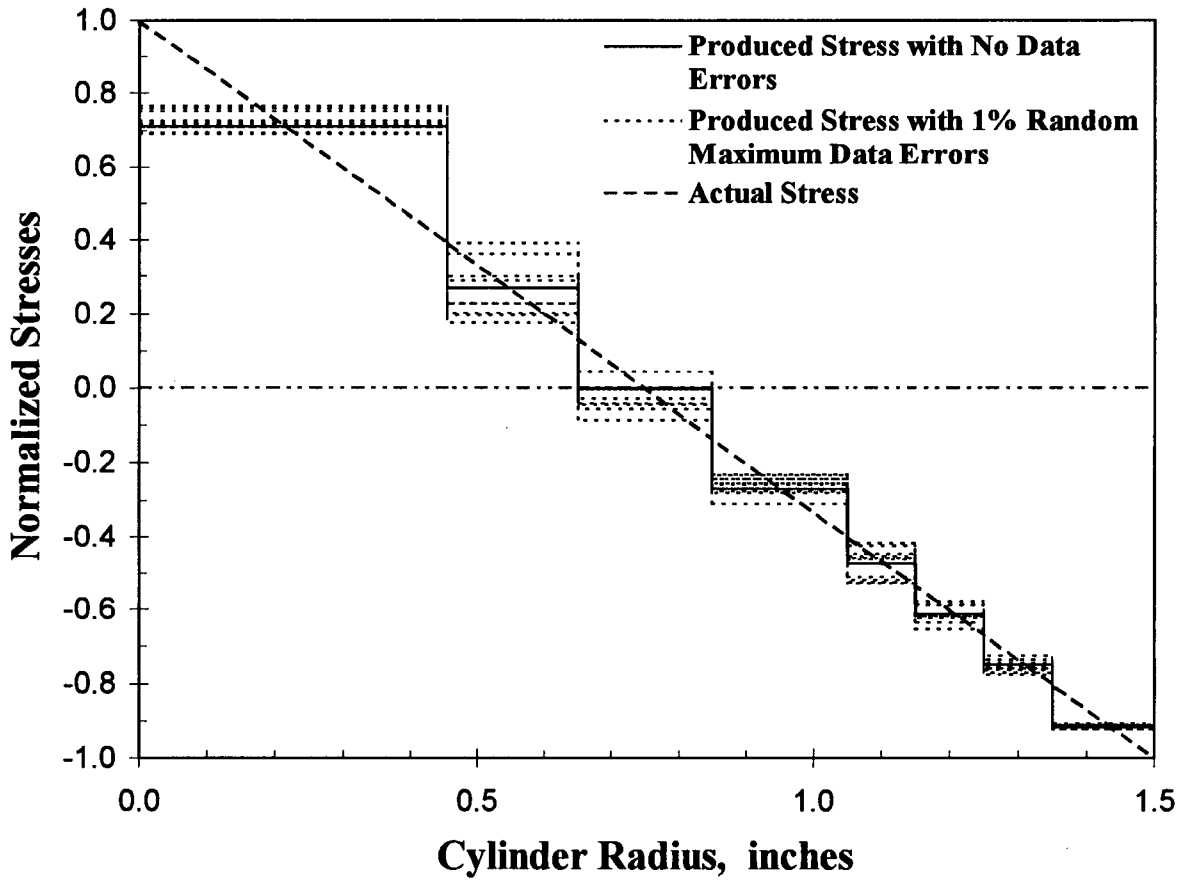

Figure 3.3 Stresses from Kernel Functions with Data Errors.

Figure 3.3 shows the ten solutions obtained from the corrupted data and the stress obtained from the ideal data. It can be seen that the solutions from the corrupted data fluctuate about the ideal solution. Each corrupted solution still obeys stress equilibrium. This requirement to obey equilibrium helps stabilize the calculated stress results.

Smoothing can be used to reduce the effect of the data errors. The added random errors in the ±1% range correspond to a standard deviation of 0.58 %. The coefficients α_j that form the stress solution were found by iteratively solving equation 2.22 to find the Lagrange multiplier μ that gives the optimal misfit specified through equation 2.17 and 2.23.

Figure 3.4 shows the smoothed stress calculation for the same 10 corrupted strain data sets used in figure 3.3. Equilibrium is still obeyed. It can be seen that the range of the produced stresses in figure 3.4 is significantly smaller than in figure 3.3. However, this reduced effect of strain data error is also accompanied by a small overall distortion of the produced stresses. This can be seen in figure 3.4 by the ideal produced stress (no smoothing no data errors) no longer being in the centre of the results from the 10 corrupted strain data sets. This is to be expected because the smoothing is achieved through a deliberate misfit between the given strain data and the produced stresses.

Figure 3.5 illustrates more clearly the distortion introduced by the smoothing procedure. The figure shows the stresses produced from ideal data (no errors), both with and

without smoothing. The shifts in the produced stresses with smoothing in figure 3.5 correspond to the median shifts observed in figure 3.4.

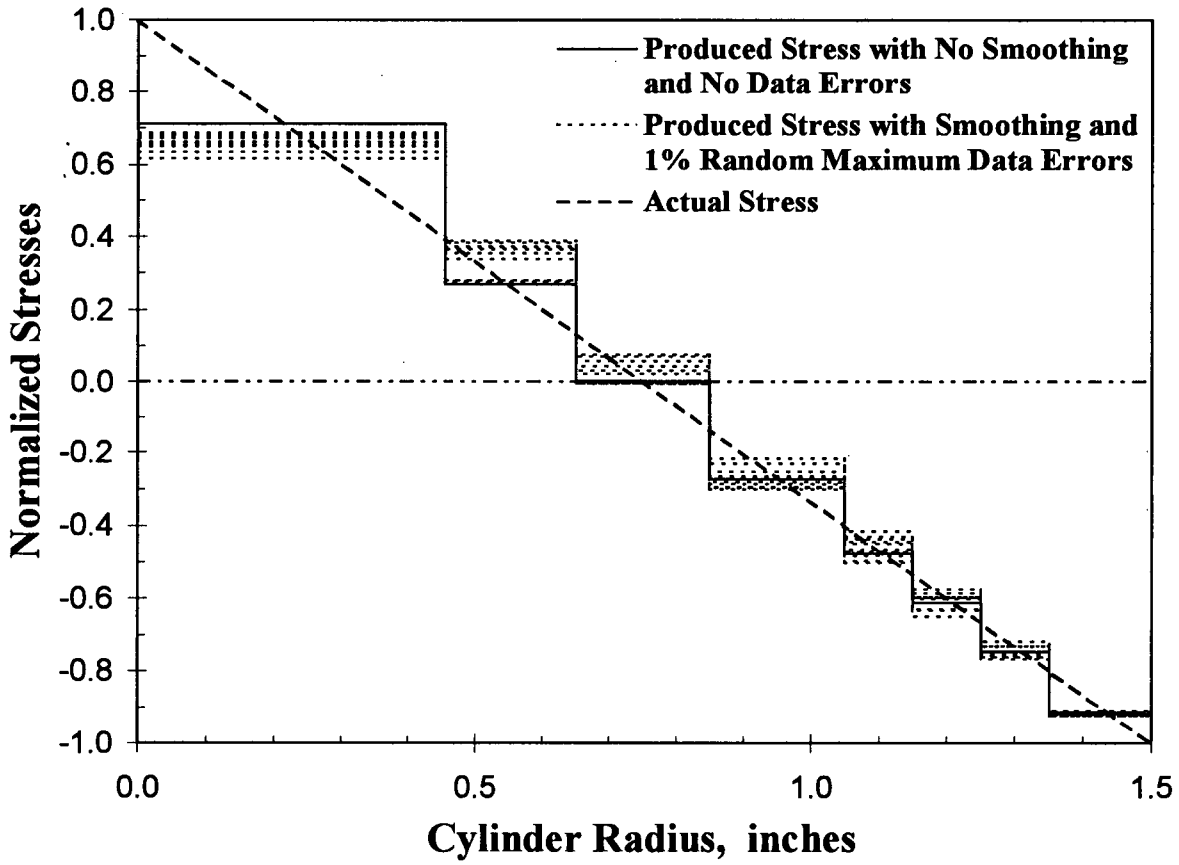

Figure 3.4 Stresses from Kernel Functions with Smoothing and Data Errors.

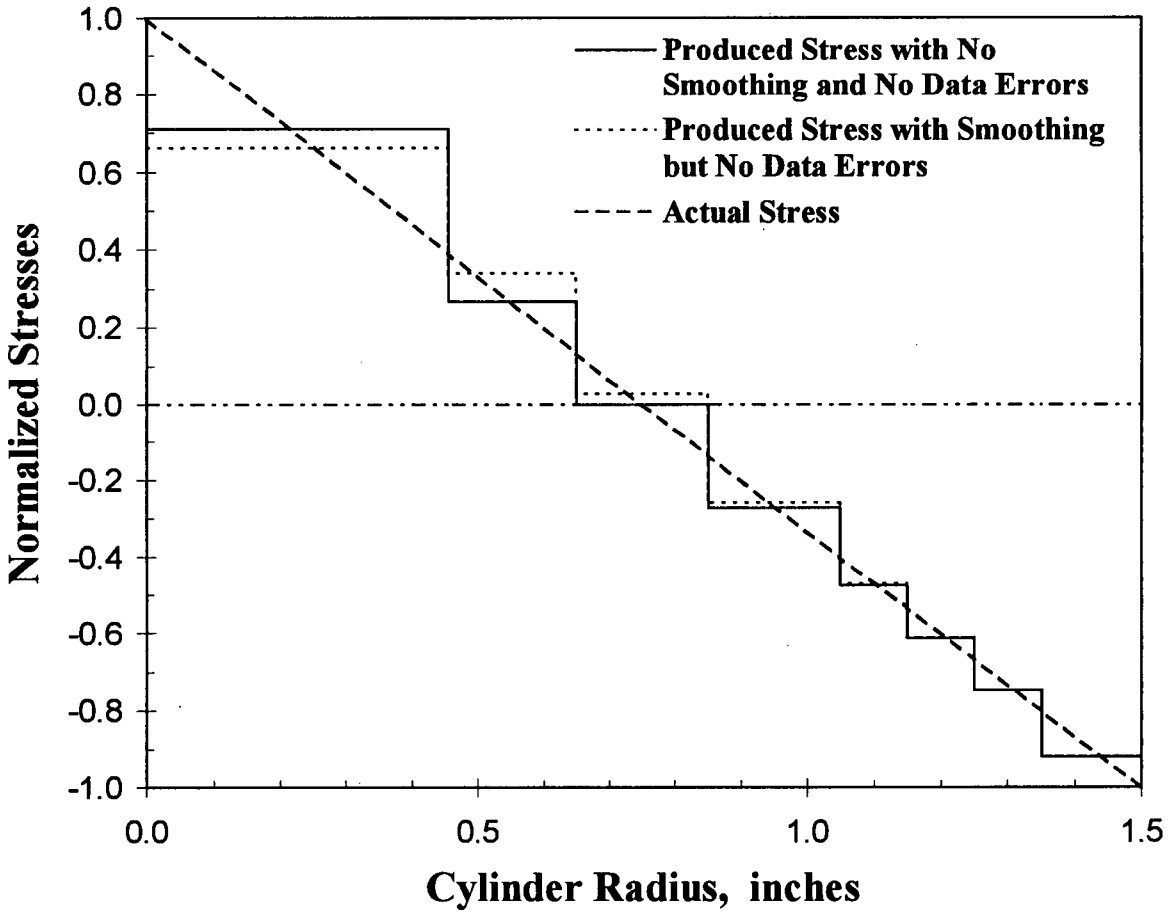

Figure 3.5 Stresses from Kernel Functions with Smoothing but No Data Errors.

Figures 3.2 to 3.5 all show that the proposed integral solution is an effective method for calculating the stresses corresponding to the measured strain data. The reliability of this calculation is enhanced by the automatic enforcement of stress equilibrium. The smoothing introduced by using deliberate data misfit reduces the effect of random data errors, but also slightly distorts the underlying solution. This behavior is common to all smoothing methods. In the calculation method presented here, the amount of smoothing is chosen to give the

statistically optimal balance between random error reduction and preservation of the underlying solution.

The results in figures 3.2 to 3.5 give a useful picture of the stress profile corresponding to the given strain data. However, the staircase shape of the lines is unrealistic. This staircase shape comes from the choice of the kernel functions $g_j(r)$ as the basis functions in equation 2.11. In the following section, some alternative basis functions will be explored that can give smoother, more realistic stress results.

3.1.2 Solution Using Power Series

The series expansion in equation 2.10 in terms of the kernel functions is mathematically convenient, but is not the only possibility. In fact, any set of independent functions that span the function space can be used. An obvious possibility is a power series.

$$\sigma_\theta(r) = \sum_{j=1}^{N} \alpha_j \, p_j \tag{3.6}$$

where

$$p_j(r) = \left(\frac{r}{r_b}\right)^{j-1} \tag{3.7}$$

These functions are shown in figure 3.6. Unlike the kernel functions, the polynomials are smooth curves.

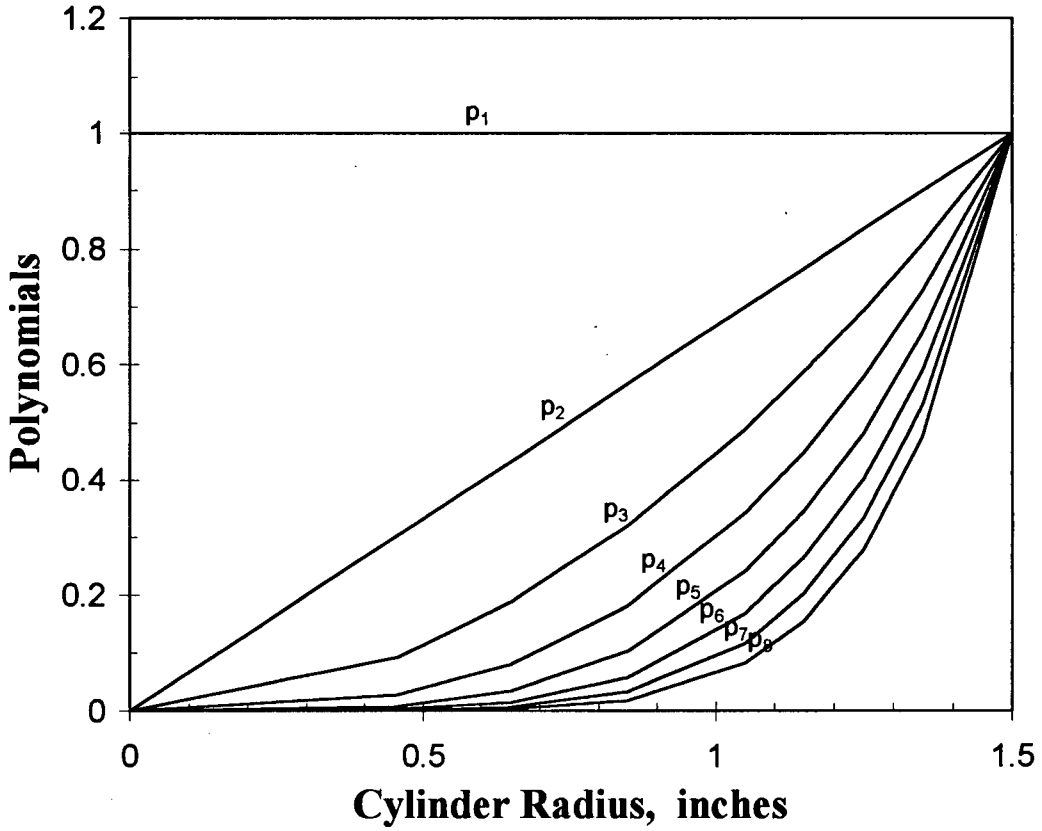

Figure 3.6 Plot of Polynomials.

The application of the power series functions changes the formulation of Γ matrix of equation 2.15. Γ becomes the inner products of the kernels and power series functions. In this case, equation 2.24 is used to determine the Γ matrix. The result is listed in table 3.2.

Table 3.2 Γ Matrix

1.0000	0.4540	0.3062	0.2242	0.1664	0.1328	0.1030	0.0712
0.6681	0.3033	0.2046	0.1498	0.1112	0.0887	0.0688	0.0476
1.0670	0.4844	0.3267	0.2393	0.1775	0.1417	0.1099	0.0760
1.6694	0.7579	0.5112	0.3743	0.2778	0.2217	0.1719	0.1188
2.7451	1.2463	0.8406	0.6155	0.4567	0.3646	0.2827	0.1954
3.7197	1.6887	1.1390	0.8340	0.6189	0.4940	0.3831	0.2648
5.4545	2.4763	1.6702	1.2230	0.9076	0.7245	0.5618	0.3883
9.4739	4.3010	2.9009	2.1242	1.5763	1.2583	0.9757	0.6744

The Γ is a non-symmetric and almost singular matrix. This is reflected in the very high condition number of the matrix. The condition number of a matrix is defined here as the ratio of the largest and the smallest eigenvalues. Since the smallest eigenvalue of the Γ matrix is almost zero, the condition number of the Γ matrix tends to infinity. By comparison, the condition number of the Γ formulated by only the kernel functions equals 547. The near-singularity of the matrix results in an unstable solution. The various stress parameters have become infinitely unrealistically large.

The Singular Value Decomposition (SVD) method [24, 25, 26] is a powerful approach for dealing with an almost singular matrix. Using SVD, the Γ matrix is decomposed into three n x n matrices: a column-orthogonal matrix U, a diagonal matrix W with positive or zero elements, and a row orthogonal matrix V:

$$\Gamma = U W V \tag{3.8}$$

In this particular case:

$$U = \begin{bmatrix} 0.0827 & 0.9504 & 0.1626 & -0.0436 & -0.2398 & -0.0547 & 0.0138 & -0.0289 \\ 0.0552 & 0.0173 & -0.1544 & 0.0171 & 0.0183 & 0.3097 & -0.0568 & -0.9344 \\ 0.0882 & 0.0713 & -0.0707 & 0.0345 & 0.2935 & 0.0875 & 0.9419 & -0.0036 \\ 0.1380 & 0.0302 & -0.0879 & 0.3082 & 0.2755 & -0.8592 & -0.0402 & -0.2481 \\ 0.2270 & 0.1451 & -0.5348 & 0.6878 & 0.0610 & 0.3036 & -0.1440 & 0.2277 \\ 0.3076 & 0.1216 & -0.5836 & -0.6519 & 0.3007 & -0.0472 & -0.1468 & 0.1041 \\ 0.4510 & 0.0431 & 0.5508 & 0.0527 & 0.6193 & 0.2338 & -0.2206 & 0.0404 \\ 0.7834 & -0.2295 & 0.0842 & -0.0284 & -0.5499 & -0.0785 & 0.1299 & -0.0171 \end{bmatrix}$$

$$W = \begin{bmatrix} 14.3657 & & & & & & & \\ & 0 & & & & & & \\ & & 0 & & & & & \\ & & & 0 & & & & \\ & & & & 0 & & & \\ & & & & & 0 & & \\ & & & & & & 0 & \\ & & & & & & & 0 \end{bmatrix}$$

$$V = \begin{bmatrix} 0.8418 & -0.4893 & 0.1946 & -0.0121 & 0.0334 & -0.1115 & 0.0109 & -0.0173 \\ 0.3821 & 0.3370 & -0.6159 & -0.4523 & -0.1676 & 0.2942 & -0.1448 & 0.1446 \\ 0.2578 & 0.6645 & 0.2803 & -0.0477 & 0.5113 & -0.3214 & -0.1798 & -0.1186 \\ 0.1888 & 0.1729 & -0.3055 & 0.8476 & -0.1952 & -0.0517 & -0.283 & 0.0437 \\ 0.1401 & 0.3401 & 0.5998 & 0.0639 & -0.4468 & 0.4348 & 0.122 & 0.312 \\ 0.1118 & 0.2181 & -0.1868 & 0.0596 & -0.2057 & -0.4346 & 0.8171 & 0.0504 \\ 0.0867 & 0.0056 & -0.1123 & 0.2557 & 0.5513 & 0.6364 & 0.4289 & -0.1468 \\ 0.0599 & 0.1114 & 0.0602 & -0.0404 & -0.3540 & 0.1098 & 0.0045 & -0.9173 \end{bmatrix}$$

Notice that the diagonal matrix W has only one non-zero element here. Since U, V are orthogonal, their inverse are equal to their transposes. The inverse of diagonal matrix W is also a diagonal matrix whose elements are the reciprocals of the elements w_j. Therefore, the inverse Γ is:

$$\Gamma^{-1} = V \left[diag \left(\frac{1}{w_j} \right) \right] U^T \qquad (3.9)$$

By applying SVD, it has been shown that $\frac{1}{w_j}$ can be replaced by zero if $w_j \cong 0$ [26].

In the present case, there is only one non-zero element in the inverse W and is: $\frac{1}{w_1} = 0.0696$.

Using equations 2.16, 3.8 and 3.6, a set of stress parameters is obtained. Table 3.3 lists the solutions from the direct matrix calculation and from the solution using SVD. It can be seen that the stress obtained from SVD is much more realistic than that from the direct method. However, stress equilibrium is not obeyed since all the stress parameters are negative. The application of SVD has greatly stabilized the solution. However, the problem is so ill-conditioned that even SVD is not sufficient to achieve a useful result. Therefore, it can be concluded that a power series is not an appropriate set of basis functions to be used to solve equation 2.8.

Table 3.3 Stresses from Different Calculation Methods.

Cylinder Radius (inches)	Stress from direct method x 10^{15}	Stress from SVD
0	0.4302	-0.0857
0.455	-0.5569	-0.1006
0.65	-1.0832	-0.1097
0.85	-1.4321	-0.1222
10.5	-0.9005	-0.1392
1.15	0.1304	-0.1502
1.25	2.0602	-0.1635
1.35	5.3199	-0.1796

Some improvement could be expected by using Legendre polynomials instead of a power series. However, the improvement may not be sufficient because the orthogonality properties of the Legendre polynomials are lost when the inner product with the kernel functions is formed.

3.1.3 Solution Using Linear Functions

The third approach is to express the stresses in equation 2.10 as a combination of piecewise linear functions

$$\sigma_\theta(r) = \sum_{j=1}^{N} \alpha_j \, l_{j-1} \tag{3.10}$$

where, when j = 1 $l_1 = 1$,

and when j >1 $$l_j = \frac{r - r_{j-1}}{r_b} \tag{3.11}$$

The linear functions are plotted in figure 3.7. These linear functions are used with equation 2.24 to determine the Γ matrix. Using equation 3.10, 2.14 and 2.16, a minimum norm solution (see figure 3.8) is obtained.

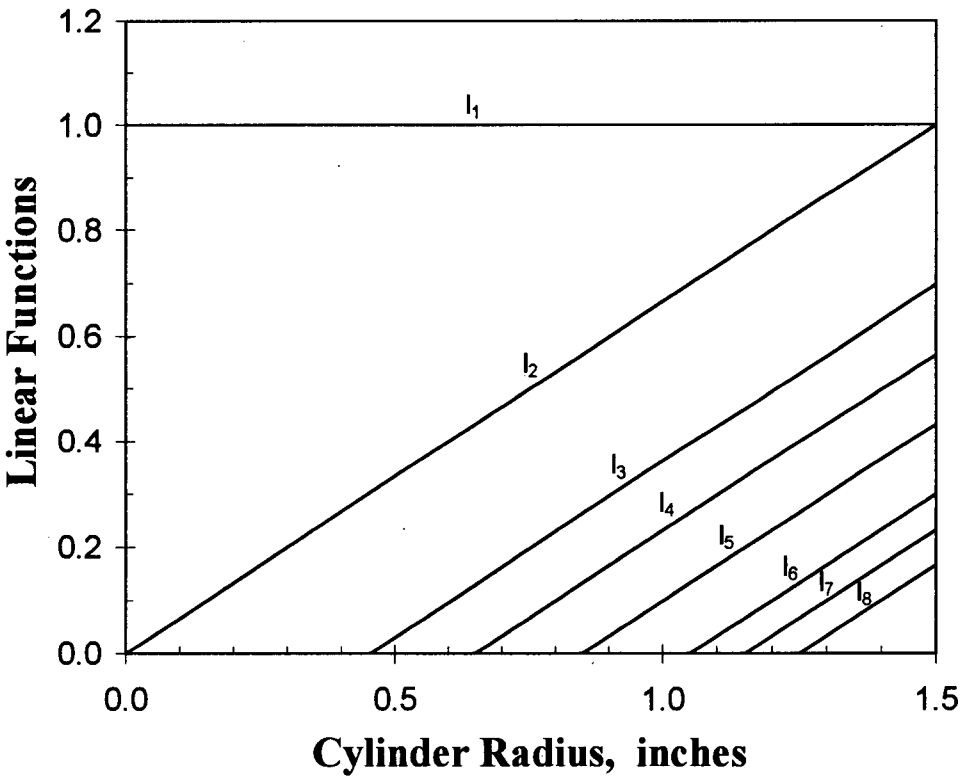

Figure 3.7 Linear Functions.

Figure 3.8 shows a plot of the stress profile produced by the linear function solution and also the actual stress. It can be seen that the linear function solution exactly coincides with the actual stress. The "exact" result is to be expected because the "actual" solution is a linear function of exactly the same type as the basis functions, and there are no data errors.

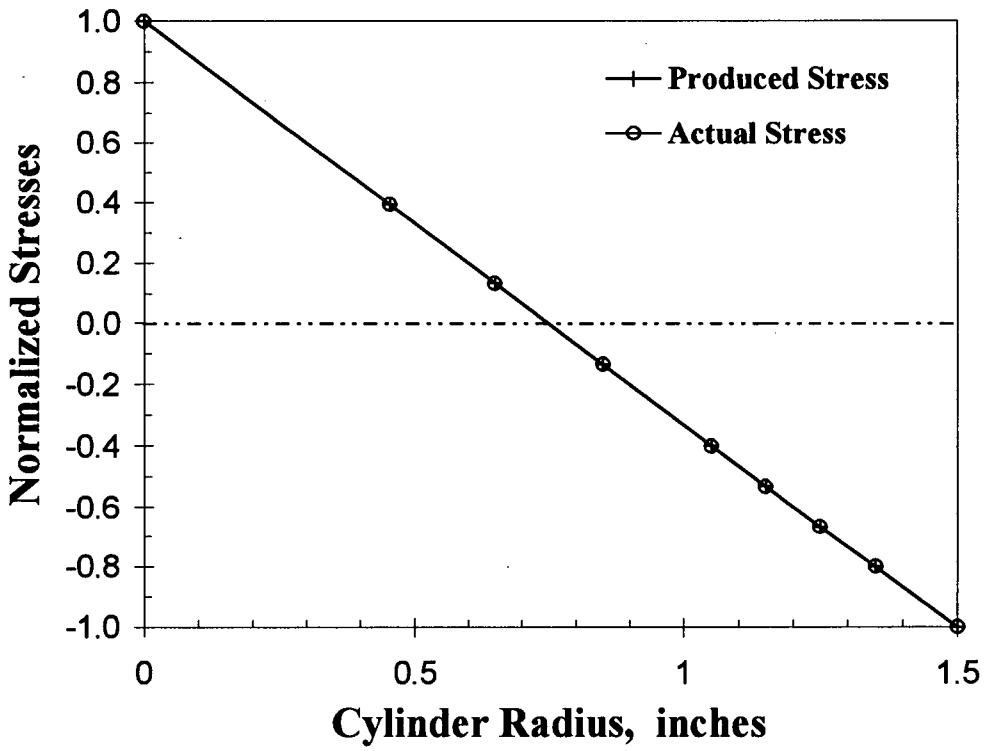

Figure 3.8 Stresses from Linear Functions with No Data Errors.

The effect of strain measurement errors was simulated in the same way as before by adding randomly selected errors in the range of ±1% of maximum strain data to each of seven non-zero strains in Table 1. Ten stress profiles were produced from the corrupted data.

Figure 3.9 shows the ten stresses from the corrupted data and the stress from the ideal data. It can be seen that the stresses in figure 3.9 from the corrupted data oscillates about the ideal stress. Each corrupted stress profile still obeys stress equilibrium. Comparing with figure 3.3 where the stresses are produced from the same type of data but are kernel function solutions, the stresses in figure 3.9 fluctuate more about the ideal stress. This shows that in this case the linear function solutions are more sensitive to errors than the kernel function solutions.

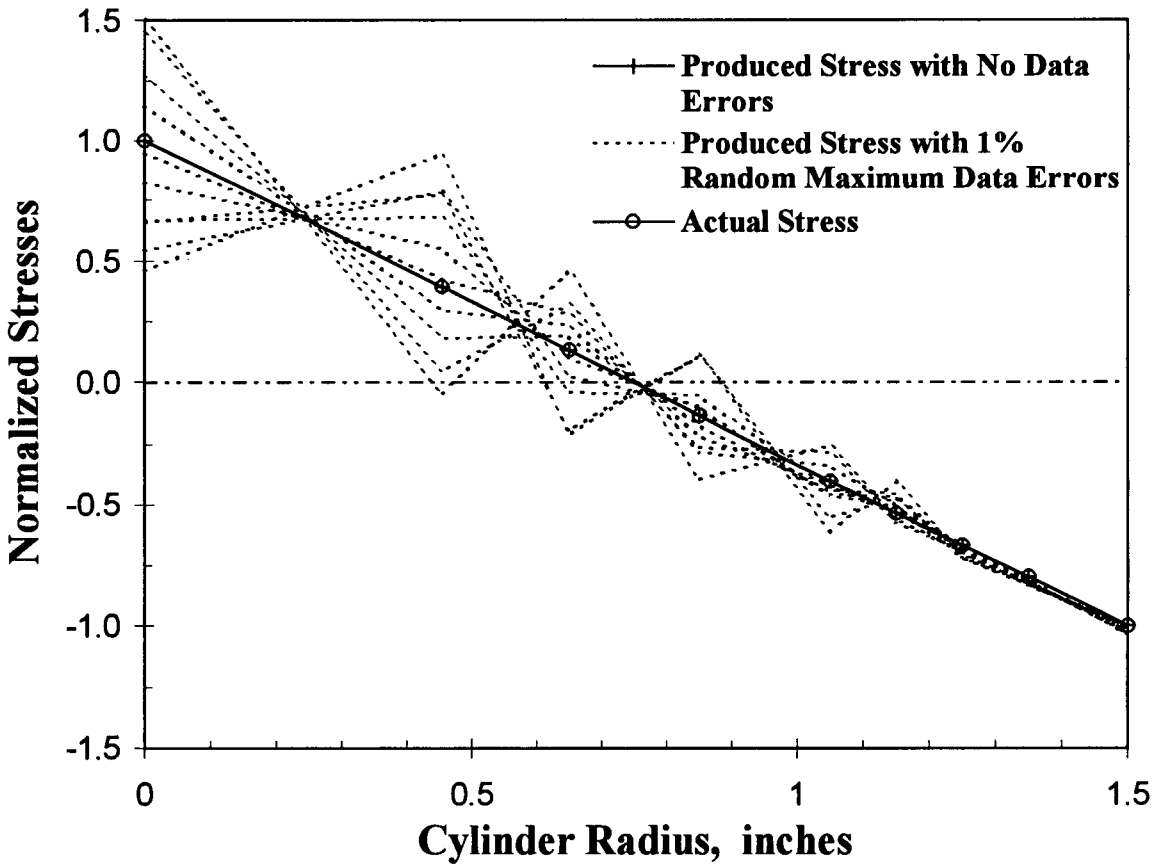

Figure 3.9 Stresses from Linear Functions with Data Errors.

Smoothing is introduced by using 0.58 % of standard deviation corresponding to the range of ±1% random maximum data errors. Equation 2.25 is used to find the coefficients α_j to form the optimum stress.

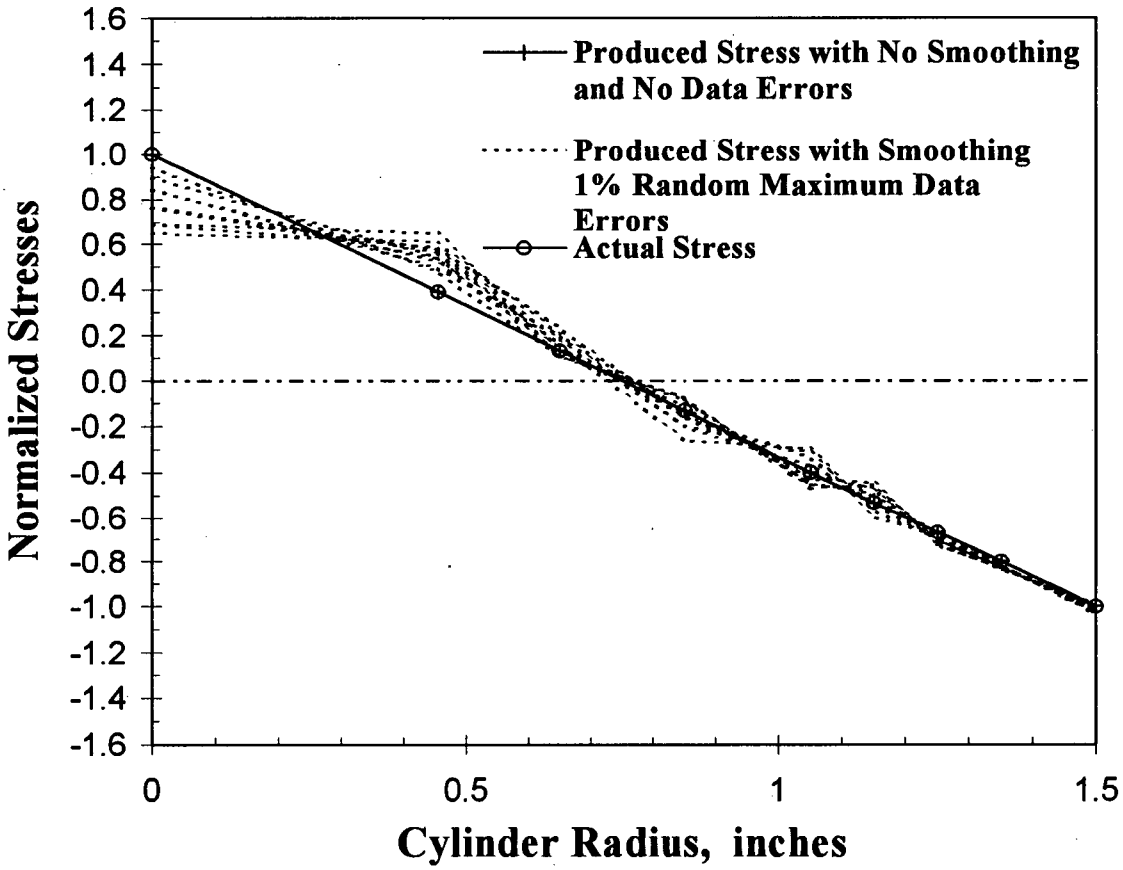

Figure 3.10 Stresses from Linear Functions with Smoothing and Data Errors.

Figure 3.10 shows ten smoothed stress solutions calculated from the same strain data sets used in figure 3.9. Stress equilibrium is still obeyed. It can be seen that the range of the smoothed stresses is much smaller than that in figure 3.9. Figure 3.10 also shows the smoothing has created some distortion. This distortion is shown more clearly in figure 3.11,

where, smoothing is applied to uncorrupted data. This corresponds to the median case in figure 3.10. Also, for a comparison, figure 3.11 shows the corresponding solution from figure 3.5 using kernel functions. It can be seen that smoothing introduces similar distortion to both kernel function and piecewise linear function solutions.

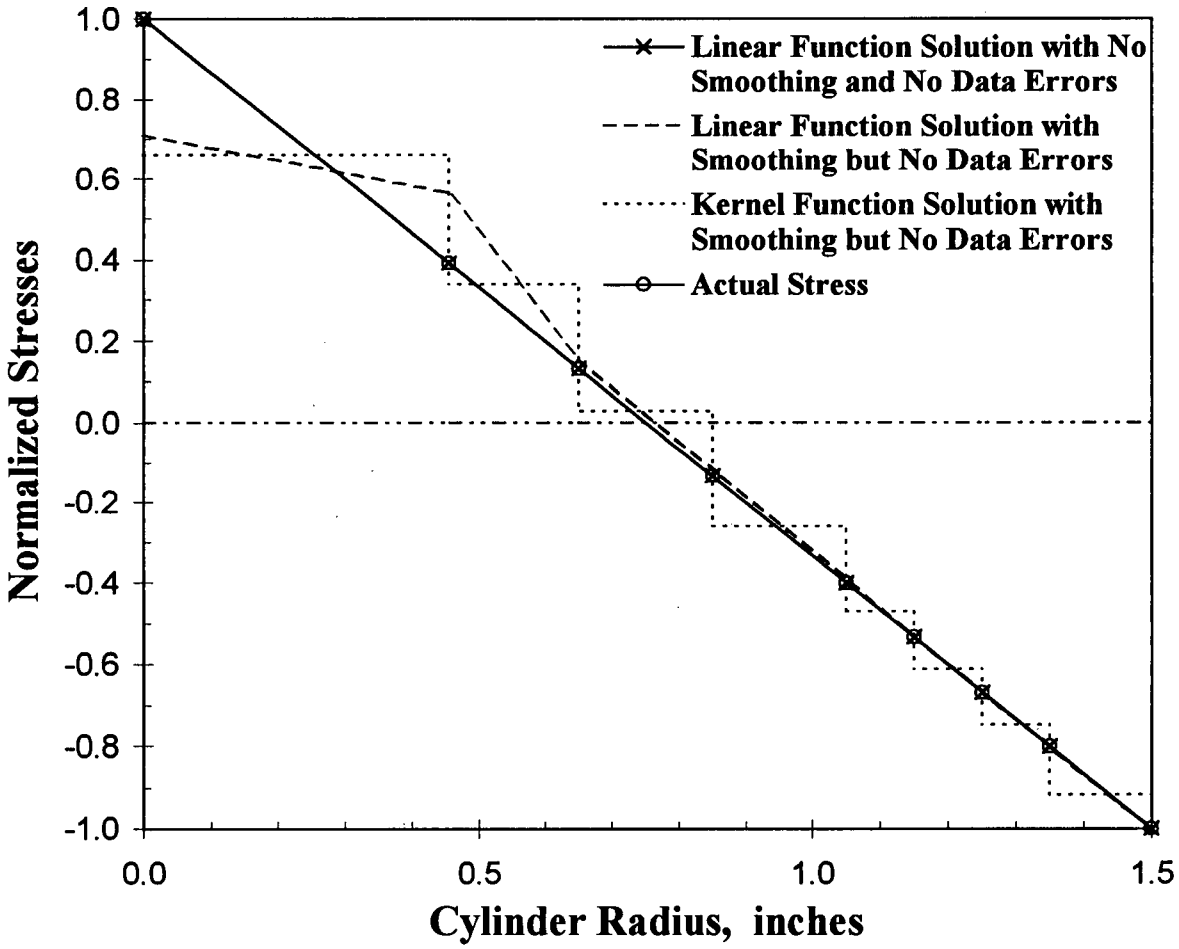

Figure 3.11 Solutions from Both Kernel Functions and Linear Functions.

The piecewise linear functions have the advantage of avoiding the unrealistic steps that occur with the kernel function solution. This advantage comes at the cost of some loss in stability. The piecewise linear solutions are locally more sensitive to strain measurement errors than the corresponding kernel function solutions. However, with appropriate smoothing, the piecewise linear solution provides a satisfactory solution.

3.1.4 Section Conclusion

This section has shown a method of applying synthetic data to solve equation 2.8. By applying synthetic data, the stability of the solution from each different basis function was explored. A good picture of the characteristics of the various basis functions was developed. The information obtained in this section will be used in the next section where the various solution methods will be applied to practical laboratory data.

3.2 Application of Laboratory Data

In this part of the chapter, laboratory data obtained by Dodd [10] are used as an example of applying linear inverse theory solving equation 2.8. Stresses obtained by Dodd using Sachs' method are also shown for comparison with the inverse solution.

The experimental data obtained by Dodd relate to the same boring operation that was used for generating the synthetic data. He measured the strain changes on the outside surface of a solid aluminum alloy cylindrical specimen, 1.5 inches in radius, caused by successive

boring out of the central part of the material. The circumferential and axial strain readings and the corresponding stresses of Sachs solution calculated by Dodd are listed in table 3.4.

Table 3.4 Laboratory Strain Readings and Sachs' Results

Radius of Bored Out Cross Section (inches)	Circumferential Strains (micro strain)	Axial Strains (micro strain)	Circumferental Stresses (ksi)
0	0	0	
0.455	-1245	-1427	4.50
0.65	-2753	-3027	1.79
0.85	-4183	-4957	0.02
1.05	-6219	-7352	-3.34
1.15	-7428	-8421	-6.56
1.25	-8262	-9176	-9.21
1.35	-8807	-9630	-10.01

Applying the inverse method to the strain readings, integral equation 2.8 is solved by the same procedure used for the synthetic data. It is assumed that the experimental data contain the range of $\pm 1\%$ of random maximum data errors. This corresponds to 0.58 % range of standard deviation for smoothing. When using kernel functions as the basis functions, stress profiles were obtained for the non-smoothed data and for the smoothed data [27].

Figure 3.12 shows the non-smoothed and smoothed inverse solutions from the experimental strain data. The staircase shape of the inverse solutions is caused by the step kernel functions. As may be expected, the smoothed solution is more evenly spaced than the non-smoothed solution. Figure 3.12 also shows the solution determined by Dodd using

Sachs' method, equation 2.1. In this particular case, the stress is smoothly varying and the results from the two methods are similar. However, the inverse solutions obey stress equilibrium.

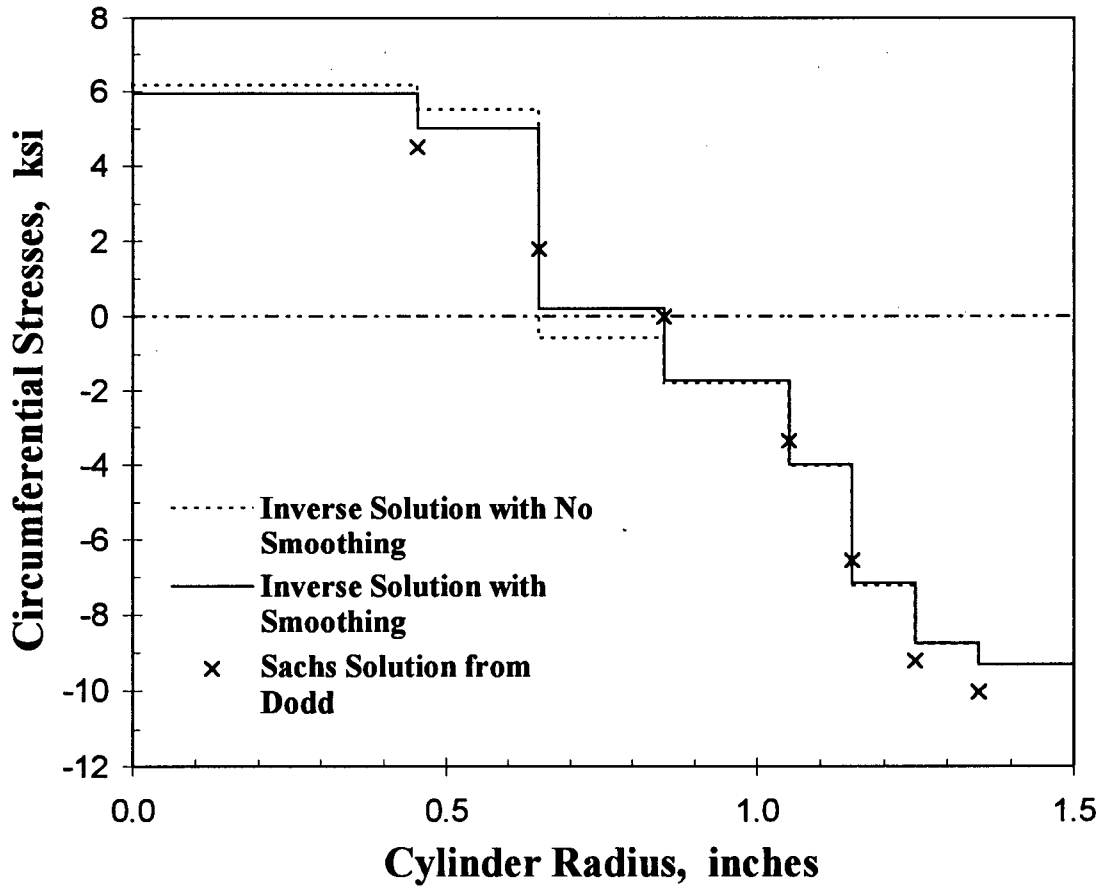

Figure 3.12 Inverse Kernel Function Solutions.

Non-smoothed and smoothed inverse solutions were also obtained using the piecewise linear basis functions. Figure 3.13 shows the two inverse solutions from the same experimental strain data used for determining the stresses in figure 3.12. It can be seen that the two inverse solutions from the linear functions are different from each other especially in

the first part of the graph. The inverse solution is realistic only in the presence of smoothing. The Sachs solution is more similar to the smoothed solution.

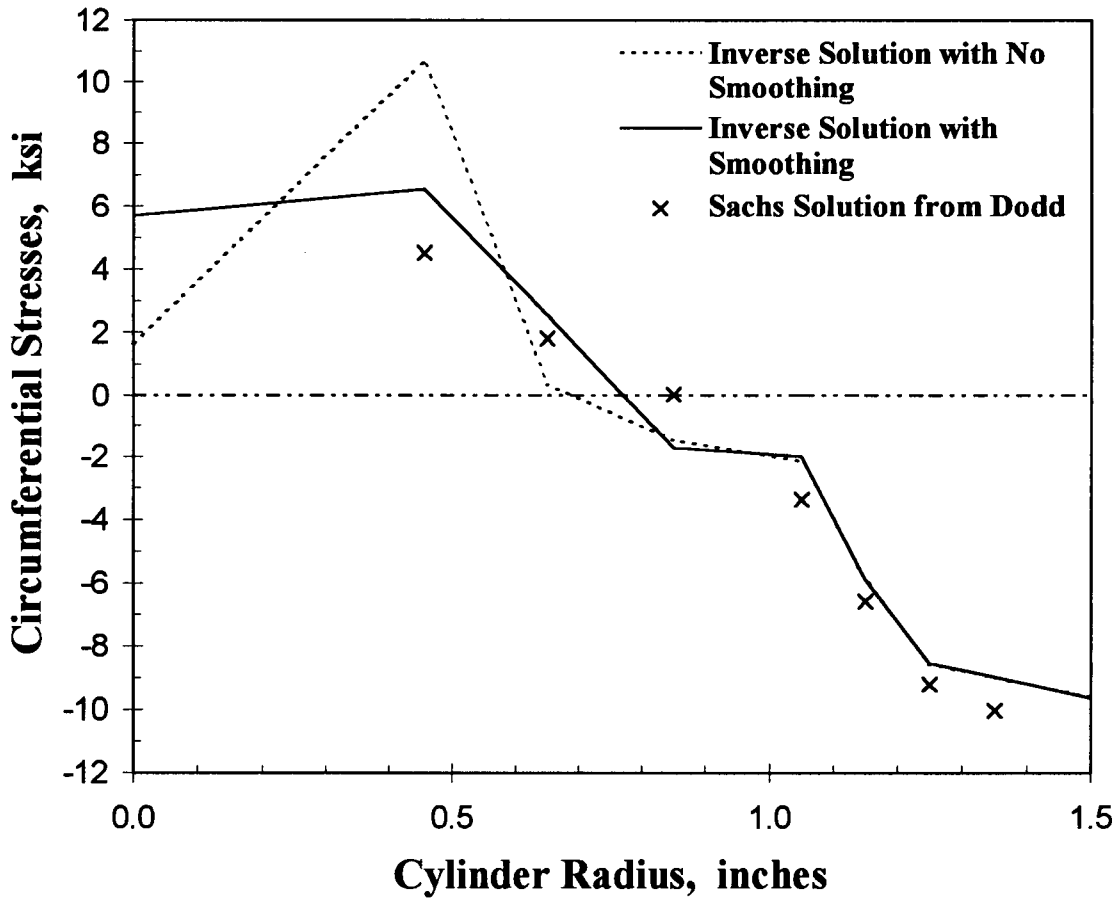

Figure 3.13 Inverse Linear Function Solutions.

Figure 3.14 shows the Sachs solution and the inverse smoothed solution for both kernel and linear functions. It can be seen that in this case the two smoothed solutions and the Sachs solution are very closely matched. This is to be expected because the actual

circumferential stress varies smoothly. The even sequence of the Sachs solution points suggests that Dodd had manually added significant smoothing during his stress calculation.

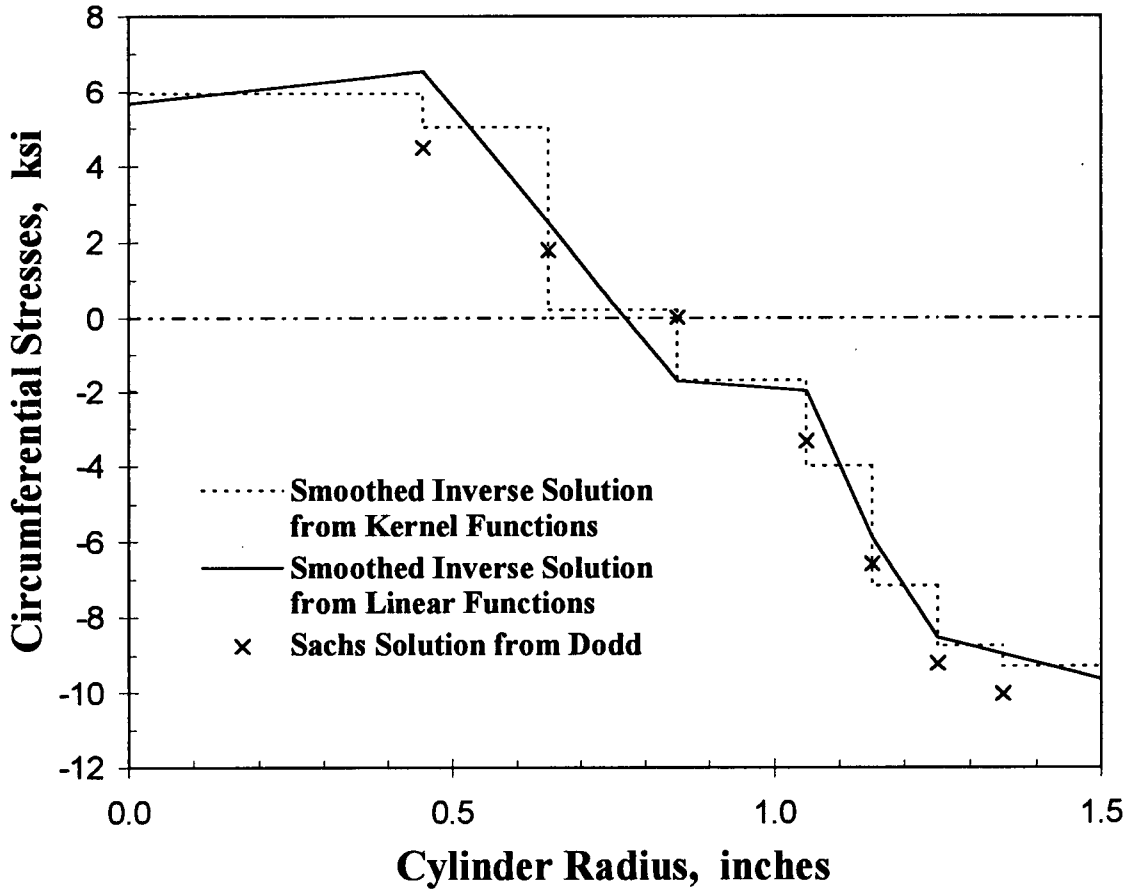

Figure 3.14 Comparison of Solution Methods Using Dodd Data.

Both the kernel function and piecewise linear functions in figure 3.14 obey stress equilibrium. This constraint is not guaranteed when using the Sachs method. The lack of enforcement of equilibrium by the Sachs method is evident in figure 3.14 by the fact that all but one of the Sachs stresses lie below the piecewise linear solution.

3.3 Chapter Conclusion

This chapter described a practical procedure for solving integral equation 2.8 using Linear Inverse Theory. Synthetic data were generated and used to illustrate how to determine the corresponding stresses. The stability of these solutions in the presence of data errors was also investigated. A method of optimal smoothing was shown to be effective in reducing the sensitivity to data errors. However, the smoothing also slightly distorted the results. Finally, the experimental data were also applied to demonstrate the practical use of the inverse method. The results from both the synthetic data and the experimental data showed that including smoothing, the inverse method is an effective and reliable method for determining residual stresses. In addition, all the inverse solutions obey stress equilibrium which the Sachs solution may fail to satisfy.

4. HOLE-DRILLING AND RING-CORE METHODS

The first part of this thesis, Chapters 2 and 3, focused on ways to improve the mathematical method for computing residual stresses from the measured strains. The second part of the thesis, Chapters 4 and 5, will focus on improving the residual stress measurement methods so that they are more sensitive to the interior stresses.

A new residual stress measurement technique, Ring-Hole Drilling, is introduced in this part of the thesis to improve the sensitivity of the measured strains to the interior stresses. The existing hole-drilling and ring-core methods have the disadvantage of being relatively insensitive to the interior stresses because the strain gauges are placed on the material surface. The new method combines aspects of both the hole-drilling and ring-core methods. However, it overcomes the interior stress resolution limitations of the two methods by moving the strain gauges from the specimen surface into the interior.

The mathematical theory of ring-hole drilling is similar to that of hole-drilling and ring-coring. This chapter summarizes the theoretical background of the hole-drilling and ring-core methods. It goes on to discuss the stress sensitivity of the two methods.

4.1 Hole-Drilling and Ring-Core Methods

The hole-drilling and ring-core methods are the most common methods for measuring residual stresses. Both involve local removal of stressed material and measurement of the resulting strain relief in the adjacent material surface. Figure 4.1 shows both the hole-drilling and ring-core methods.

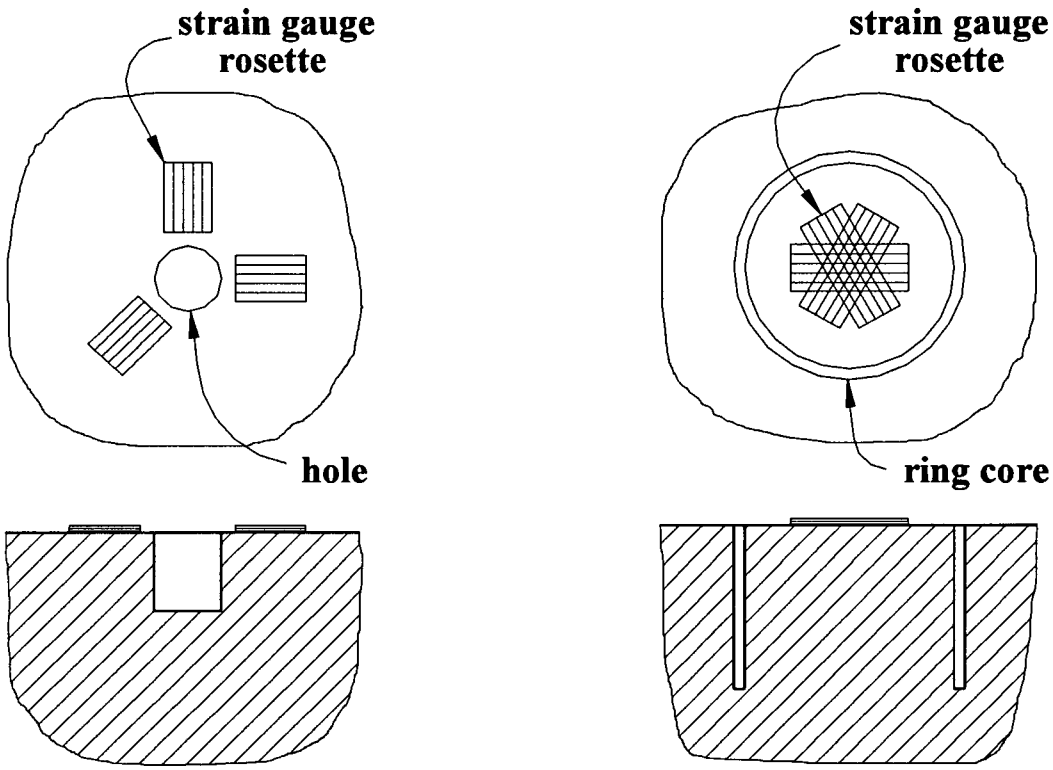

(a) Hole-Drilling Method (b) Ring-Core Method

Figure 4.1 Hole-Drilling and Ring-Core Methods.

4.2 Hole-Drilling

The hole-drilling method involves drilling a small hole, typically 0.040-0.200 inches (1-5 mm) in diameter and depth, in the centre of a specially designed strain gauge rosette attached to the surface of the stressed material (see figure 4.1(a)). Strain measurements are then taken as the hole depth is increased by small increments. The original residual stresses can then be calculated from the measured strains.

The hole-drilling method can be used for uniform and non-uniform residual stress measurements. In many cases, the residual stress can be assumed to be uniform through the depth of the material. This assumption greatly simplifies the calculation procedure. However, often the stresses are quite non-uniform. In that case, a more complex, non-uniform stress calculation is required.

4.2.1 Uniform Residual Stress

The relationship between the measured relieved strain and the originally existing residual stresses is [13, 17]:

$$\varepsilon_r = A\left(\sigma_{max} + \sigma_{min}\right) + B\left(\sigma_{max} - \sigma_{min}\right)\cos 2\gamma \qquad (4.1)$$

where, ε_r is the measured relieved radial strain, σ_{max} and σ_{min} are the maximum and minimum principal residual stresses respectively. γ is the angular coordinate measured anticlockwise from the maximum principal stress direction. A and B are the calibration coefficients to be determined.

Equation 4.1 can be inverted to obtain the magnitude and direction of the two principal stresses in terms of the measured strains:

$$\sigma_{max}, \sigma_{min} = \frac{\varepsilon_1 + \varepsilon_3}{4A} \mp \frac{\sqrt{(2\varepsilon_2 - \varepsilon_1 - \varepsilon_3)^2 + (\varepsilon_1 - \varepsilon_3)^2}}{4B} \tag{4.2}$$

$$\beta = \frac{1}{2} \arctan \frac{2\varepsilon_2 - \varepsilon_1 + \varepsilon_3}{\varepsilon_1 - \varepsilon_3} \tag{4.3}$$

where ε_1, ε_2 and ε_3 are the radial strains measured by the strain gauges showed in figure 4.1 and β is the angle measured clockwise from gauge 3 to the maximum principal stress direction.

For a thin wide plate subjected to uniform stress, the coefficients A and B in equation 4.1 can be determined as [2]:

$$A = -\frac{1+\nu}{2E}\left(\frac{r_a}{r}\right)^2 \tag{4.4}$$

$$B = -\frac{1+\nu}{2E}\left(\frac{4}{1+\nu}\left(\frac{r_a}{r}\right)^2 - 3\left(\frac{r_a}{r}\right)^4\right) \tag{4.5}$$

where r_a is the hole radius and r is the generalized radius and $r < r_a$. A and B obtained in this way refers to strains measured at a point at the centre of the strain gauge. However, the

strains actually vary over the entire strain gauge area. For more accurate residual stress calculation, an integration over the strain gauge area is needed [29]. The coefficients calculated in this way are designated as $\overline{A}$ and $\overline{B}$, and differ from A and B by up to 20%.

The preceding calculation of A and B or $\overline{A}$ and $\overline{B}$ is often not practical because most test objects are machine parts and structures and they are rarely thin or flat. Therefore, a shallow "blind" hole is used for testing residual stresses in the material. For the blind hole test, equation 4.1 still applies, but wih slightly different values of $\overline{A}$ and $\overline{B}$ [2]. However, the determination of $\overline{A}$ and $\overline{B}$ for the blind hole is more complex. It requires either experimental or finite element calibrations.

In most cases, experimental calibration of $\overline{A}$ and $\overline{B}$ is accomplished by a tensile or compressive test on a separate specimen. The test involves installing a strain gauge rosette on the specimen surface, subjecting the specimen to a known uniform stress field and measuring the rosette strains before and after hole drilling. The coefficients $\overline{A}$ and $\overline{B}$ can then be calculated from the measured strains [15]. This type of experimental calibration has the advantage of being conceptually simple. Its main disadvantage is that the calibration must be repeated for every different set of geometric parameters of the materials [15].

The application of the finite element calculations to residual stress measurement simplifies the numerical calibration coefficients $\overline{A}$ and $\overline{B}$. The finite element calibration is more general and covers a wide range of measurement conditions. The results match

experimental calibrations well. Therefore, the finite element calibration is widely accepted and used.

The theoretical approach for the finite element calibration is based on the superposition of the stresses in the material [17]. Assume that the boundary of the material is sufficiently far from the hole so the effects of drilling a hole can be neglected at the boundary. The initial stresses at the hole are further assumed to be uniform so there are no shear stresses at the hole surface.

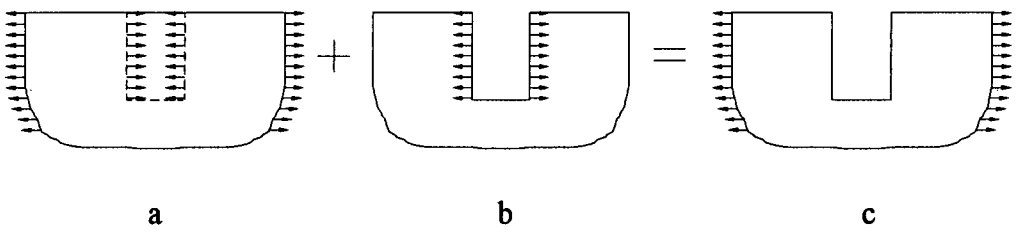

Figure 4.2 Superposition of the Stresses to Find the Strain Relaxation due to Hole-Drilling.

Figure 4.2 shows a schematic of the stress state in a specimen both before and after hole-drilling. Figure 4.2(a) shows the stresses existing before hole-drilling. These stresses are indicated at the hole surface. Equal and opposite stresses are shown in figure 4.2(b), corresponding to the stresses relieved by the hole-drilling. Figure 4.2(c) shows the sum of the stresses in figures 4.2(a) and 4.2(b). This latter diagram shows the stress state after hole-drilling. The displacements around the hole caused by the stresses in figure 4.2(b) can be

modeled by the finite element method. These displacements can then be numerically integrated over the active strain gauge area to simulate the measured strains [29]. Substituting the calculated strain and the known stresses in equation 4.1, the coefficients $\overline{A}$ and $\overline{B}$ can be determined.

The coefficients $\overline{A}$ and $\overline{B}$ can be explicitly determined from equation 4.1 [17, 30]. To obtain $\overline{A}$, apply a hydrostatic stress $\sigma_{max} = \sigma_{min} = 1$, which gives:

$$\overline{A} = \frac{\varepsilon_h}{2} \tag{4.6}$$

where ε_h is average strain over the strain gauge grid area corresponding to the applied stresses. Coefficient $\overline{B}$ can be calculated by applying a shear stress $\sigma_{max} = -\sigma_{min} = 1$:

$$\overline{B} = \frac{\varepsilon_s}{2\cos 2\gamma} \tag{4.7}$$

where ε_s is the average strain corresponding to the shear stresses and γ is the angle between the strain gauge mid radial axis and the principal stress direction.

The values of the calibration coefficients $\overline{A}$ and $\overline{B}$ depend on the geometry of the hole and the strain gauge and the specimen material properties, Poisson's ratio and modulus of elasticity. To avoid determining $\overline{A}$ and $\overline{B}$ for each material, the material property

dependency must be eliminated. This can be achieved by introducing two dimensionless calibration coefficients $\bar{a}$ and $\bar{b}$ [17]:

$$\bar{a} = \frac{2E\bar{A}}{1+\nu} \tag{4.8}$$

$$\bar{b} = 2E\bar{B} \tag{4.9}$$

Equation 4.1 and 4.2 can be written in terms of these two dimensionless constants:

$$\varepsilon = \frac{(1+\nu)\bar{a}}{E}\frac{(\sigma_{max}+\sigma_{min})}{2} + \frac{\bar{b}}{E}\frac{(\sigma_{max}-\sigma_{min})}{2}\cos 2\gamma \tag{4.10}$$

$$\sigma_{max}, \sigma_{min} = \frac{E}{(1+\nu)}\frac{(\varepsilon_1+\varepsilon_2)}{2\bar{a}} \mp \frac{E\sqrt{(2\varepsilon_2-\varepsilon_1-\varepsilon_3)^2+(\varepsilon_1-\varepsilon_3)^2}}{2\bar{b}} \tag{4.11}$$

By normalizing the hole radius r and depth h with respect to the strain gauge mean radius r_m, the calibration coefficients $\bar{a}$ and $\bar{b}$ become approximately proportional to the square of the normalized hole radius [17, 18]. Figure 4.3 shows the variation of $\bar{a}$ and $\bar{b}$ vs. normalized hole depth for a normalized hole radius of $r/r_m = 0.5$ [17]. The corresponding values of $\bar{A}$ and $\bar{B}$ for a given material can be determined through equations 4.8 and 4.9. Residual stresses can then be evaluated from equation 4.2 by substituting the coefficients $\bar{A}$ and $\bar{B}$.

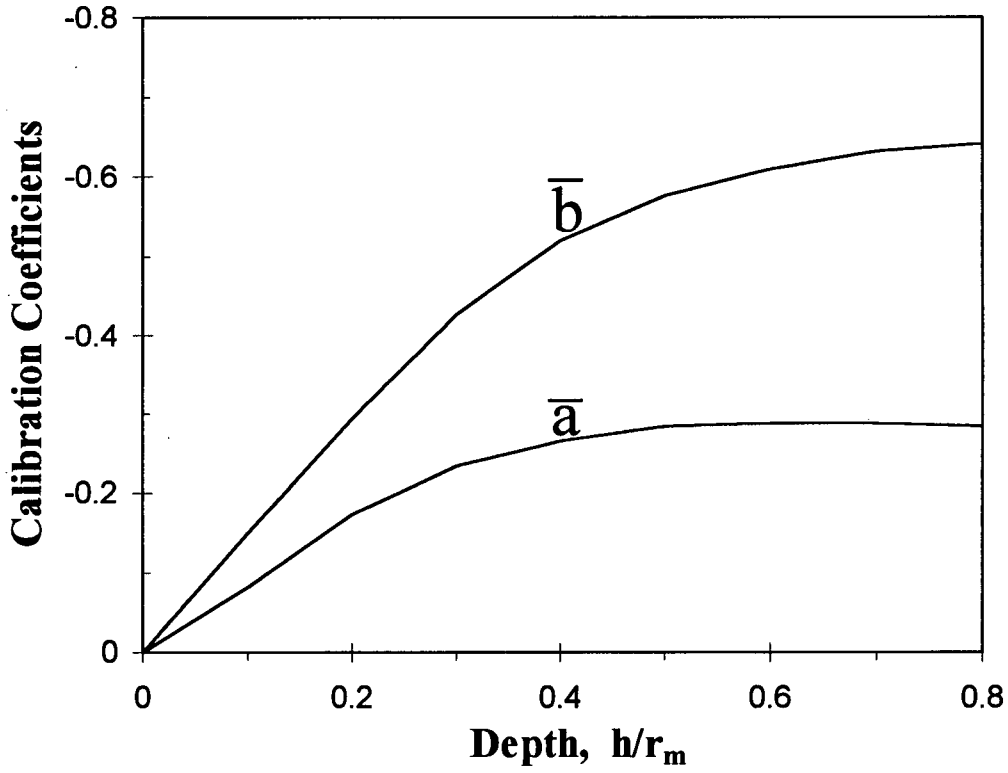

Figure 4.3 Calibration Coefficients for the Hole-Drilling Method for $r_a/r_m = 0.5$.

4.2.2 Non-Uniform Residual Stress

In many cases, the residual stress are non-uniformly distributed through the material. The stress non-uniformity complicates the residual stress calculation. Of the various available calculation methods, the Integral method is the most general [18].

When using the Integral method, the strains measured during the hole drilling are the cumulative result of relieving the residual stresses originally existing at all depth locations

within the total hole depth. The individual contributions of the stresses at each depth location to the total measured strains are identified and the individual stresses are calculated from these total strain measurements [16, 18].

4.3 Ring-Core Method

The ring-core method is similar to hole-drilling, but with an opposite configuration. Hole-drilling involves drilling a hole in the centre of a strain gauge rosette. Ring-core drilling involves milling a ring-core around the outside of a strain gauge rosette. The ring-core is typically 0.600-6.000 inches (15-150 mm) in diameter and depth. The relieved strains are measured by strain gauges attached on the top surface of the core (see figure 4.1(b)). The original residual stresses can then be calculated from the measured strains in the same way as with the hole-drilling method.

The ring-core method has higher sensitivity than the hole-drilling method because it involves almost complete strain relief. However, the sensitivity to interior stresses is also quite modest. The theoretical calculations of the ring-core method are similar to the hole-drilling method. A complete theoretical approach was given by Wolfgang et al. and other researchers [22, 31].

4.4 Strain Sensitivity of the Hole-Drilling and Ring-Core Methods

The strain sensitivity of the hole-drilling and ring-core methods is defined as the relieved strain per unit residual stress. Larger strain sensitivity is desired so that the strain

measurement errors do not significantly affect the calculation results. The strain sensitivity, is quantified through the calibration coefficients $\bar{a}$ and $\bar{b}$. Larger calibration coefficients result in higher strain sensitivity, and hence greater resistance to the effects of strain measurement errors.

The strain sensitivity of the hole-drilling method is low. The main reason is that the material underneath the gauges is subjected only to partial strain relief. In the case of the ring-core method, the material under the gauges experiences complete strain relief. The corresponding maximum value of the calibration coefficients are:

$$\bar{a} = \frac{1-\nu}{1+\nu} = 0.54 \quad \text{for } \nu = 0.3 \tag{4.12}$$

$$\bar{b} = 1+\nu = 1.3 \quad \text{for } \nu = 0.3 \tag{4.13}$$

The maximum value of coefficients for hole-drilling is much lower, they only can reach half of that of the ring-core (see figure 4.3).

Low strain sensitivity of the hole-drilling method diminishes the reliability of the calculated residual stresses. This is because low strain sensitivity reduces the size of the measured strains relative to that of the strain measurement errors. In the past, many researchers have tried to improve the sensitivity of the two methods by modifying the size and the shape of the hole for the hole-drilling and by modifying the size and the shape of the ring core for the ring-core method [32, 33]. However, the improvements that can be achieved by

these mehods are limited because the essential problem of both methods is that the strain gauges are located on the surface of the material and are too far away from the interior stresses. In the next chapter, a new method, ring-hole drilling, will be introduced in detail. The new method overcomes the low sensitivity of both hole-drilling and ring-core methods and is a practical method for measuring residual stresses.

5. RING-HOLE DRILLING

This chapter introduces in detail a new residual stress measurement method, Ring-Hole Drilling. The existing hole-drilling and ring-core methods have the disadvantage of being insensitive to interior stresses because the strain gauges are placed on the material surface, far from the interior. The proposed method overcomes this limitation by moving the strain gauges from the surface to the interior of the material. This chapter describes the proposed method and its theoretical background. It also demonstrates that the new method is a practical technique for measuring residual stresses in a material.

5.1 Ring-Hole Drilling

Ring-hole drilling involves drilling a small hole at the desired test location, inserting strain gauges in the hole and milling an annular ring incrementally around the hole. Figure 5.1 shows a cross-section view of the ring and the hole made during ring-hole drilling. The strain changes caused by milling the annular ring are then measured by the strain gauges, from which the residual stresses that originally existed in the material can be calculated.

The theory of ring-hole drilling is similar to that of the hole-drilling and the ring-core methods described in Chapter 4. It differs only in the numerical values of the calibration coefficients $\bar{a}$ and $\bar{b}$. These coefficients can be determined by either experimental or finite element procedures. Both procedures are described in this chapter and the results of the two methods are compared.

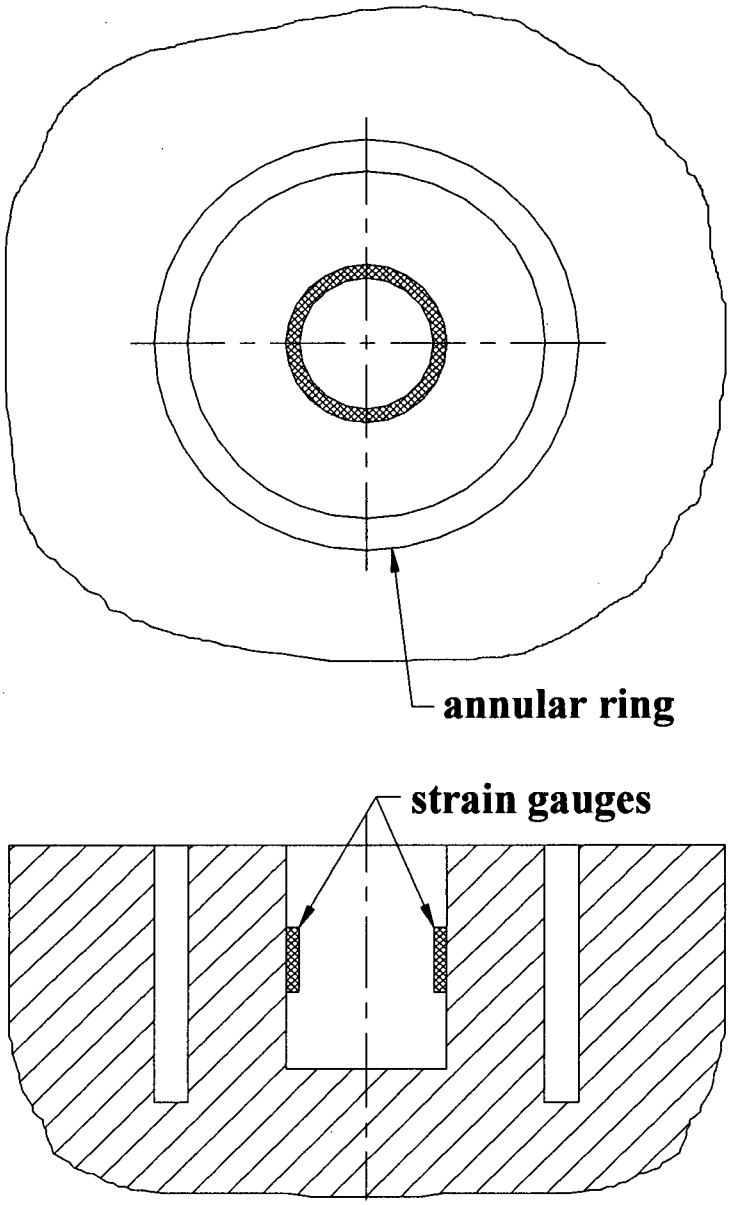

Figure 5.1 Cross-Section of the Ring and the Hole of Ring-Hole Drilling.

5.2 Finite Element Calibration Method

Calculation of the calibration coefficients $\bar{a}$ and $\bar{b}$ using the finite element method is based on a superposition of the stresses in the material [17]. Assume that the boundary of the material is sufficiently far from the hole and ring that their effects can be neglected at the boundary. The initial stresses in the material are further assumed to be uniform so there are no shear stresses at the hole surface.

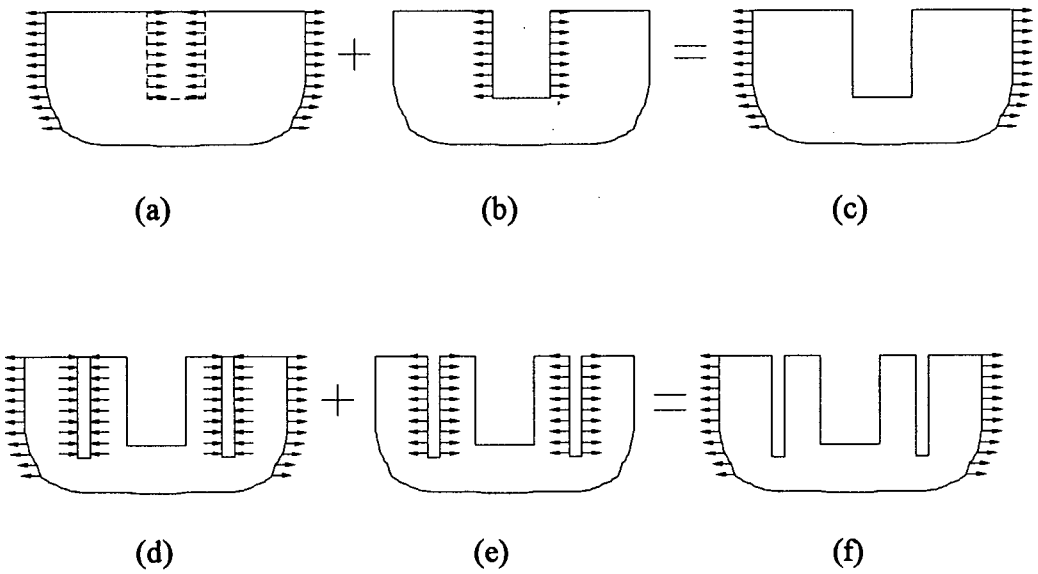

Figure 5.2 Superposition of the Stresses to Find the Strain Relaxation Caused by Milling a Ring.

Figure 5.2 shows a schematic of the stress state in a specimen both before and after cutting a hole and a ring. Figure 5.2(a) shows the stresses existing at the hole location before drilling the hole. If the hole is drilled, and conceptually the original stresses are replaced at the

hole boundary, then there will be no stress change in the surrounding material. Figure 5.2(c) shows the stress state existing after the hole drilling. By superposition, the difference between the stress states before and after hole drilling is represented by Figure 5.2(b). Here, the opposites of the original residual stresses are applied at the hole boundary. This case corresponds to the deformations resulting from hole drilling.

A similar discussion applies to figures 5.2(d)-(f). Figure 5.2(d) corresponds to the stresses that exist after hole drilling but before ring milling. Figure 5.2(f) corresponds to the stresses that exist after hole drilling and ring milling. Figure 5.2(e) is the case of particular interest because it corresponds to the deformations measured during ring milling. The stress states in figure 5.2(c) is the same as in Figure 5.2(d). The only difference between the two diagrams is that the second one explicitly shows the stresses at the ring location, while the first does not.

The deformations caused by ring milling can be calculated by doing a finite element analysis of the structure in Figure 5.2(e). The stresses on the loaded faces of the ring need to be determined first by doing a separate finite element analysis of the structure in Figure 5.2(b) and then adding the original residual stresses from Figure 5.2(a). The displacements determined in this way can then be numerically integrated over the active strain gauge area to evaluate the measured strains [29]. By substituting these strains and the original residual stresses in equation 4.1, the coefficients $\bar{a}$ and $\bar{b}$ for Ring-Hole drilling can then be determined.

5.3 Finite Element Results

Figure 5.3 shows the finite element mesh used for the ring-hole drilling calculations. It has 994 nodes and 941 elements. The depth of the ring is adjusted during various calculations by assigning a near zero elastic modulus to the elements within the desired ring depth. Due to symmetry, only half of the material need be meshed to complete the calculations [18].

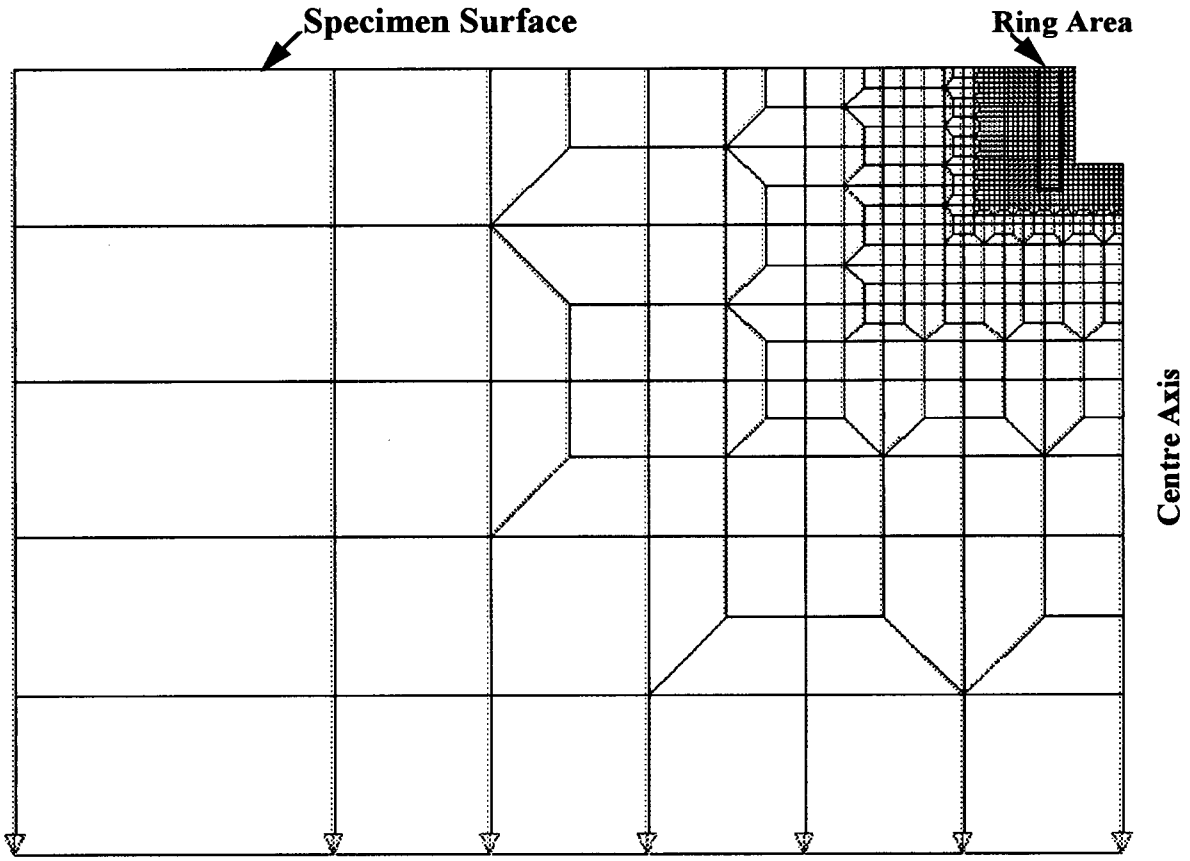

Figure 5.3 The Finite Element Mesh Used for Strain Relaxation Calculations.

Figures 5.4 and 5.5 show some example finite element calculations of the calibration coefficients $\bar{a}$ and $\bar{b}$ for ring-hole drilling. These two graphs illustrate the effect of three fundamental factors that influence the relieved strains. They are: ring depth, ring inner diameter and strain gauge depth. Figure 5.4 illustrates the influence of the first two of these factors for a fixed strain gauge depth of 0.156". As may be expected, both calibration coefficients increase with increase in ring depth. From consideration of St. Venant's principle [34], it may be expected that the influence of cutting the ring should be felt over a depth similar to the wall thickness. This can be seen clearly for coefficient $\bar{a}$, where a rapid change in value occurs for small ring diameters. The change occurs over increasingly large depth ranges for the larger ring diameters. The curves for $\bar{b}$ do not show this behavior so clearly. This is because they are also greatly affected by the material at the bottom of the hole which stiffens the surrounding area and inhibits full strain relief. As a result, the various $\bar{b}$ curves do not closely approach their theoretical assympotic value of 4. This stiffening effect is less prominent on calibration coefficient $\bar{a}$.

Figure 5.5 shows the influence of strain gauge depth on the calibration coefficients $\bar{a}$ and $\bar{b}$ for a fixed ring inner diameter of 0.75". Again, as may be expected from St. Venant's Principle, the greatest variation in the coefficients is expected when the ring depth is similar to the strain gauge depth. As before, calibration coefficient $\bar{a}$ shows this behavior most clearly. Its value rises rapidly at small ring depths when the strain gauges are near the surface. The coefficient rises at greater ring depths when the strain gauges are fixed deeper in

the hole. Again, the stiffening effect of the material at the bottom of the hole is apparent. The deeper the strain gauges go, the nearer they get to the stiffened region at the bottom of the hole, and the smaller the value of $\bar{a}$ becomes. Calibration coefficient $\bar{b}$ behaves in generally the same way as coefficient $\bar{a}$, but the trends are again masked by the stiffening effect of the material at the bottom of the hole.

From Figures 5.4 and 5.5, it can be concluded that ring-hole drilling increases the calibration coefficients $\bar{a}$ and $\bar{b}$ dramatically. The graphs show that the maximum values of $\bar{a}$ and $\bar{b}$ reach about 2 and 3.5 respectively. These values represent an increase in $\bar{a}$ and $\bar{b}$ of 270% and 170% respectively when compared with the ring-core method, and more than double these factors when compared with the hole-drilling method. The main reason for the high values of the two calibration coefficients is the stress concentration created by the presence of the hole. The strain gauges measure the corresponding strains. The measured strain sensitivity is therefore much greater than the ring-core method. The strain gauges also measure almost the entire relieved strains, and therefore they provide a much greater strain sensitivity than the hole-drilling method, when only a small fraction of the relieved strains are measured.

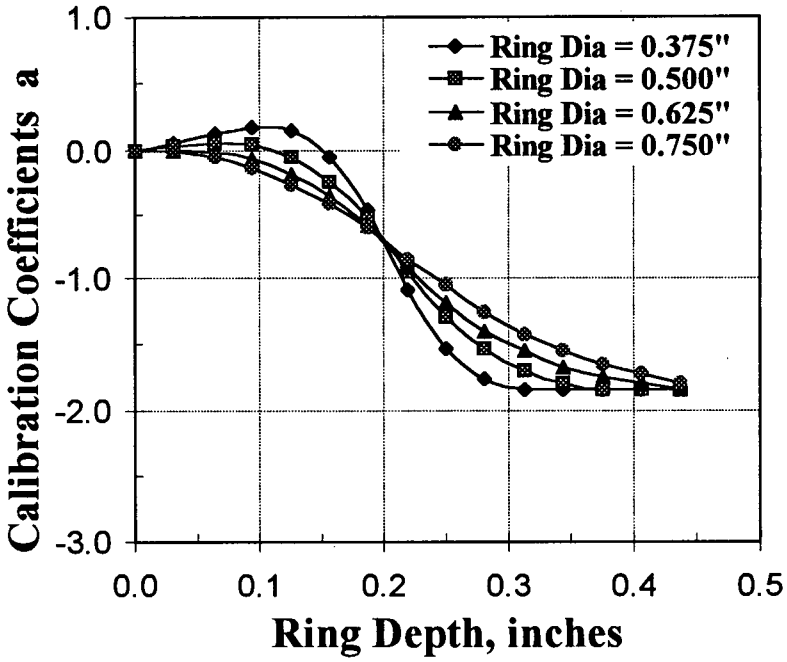

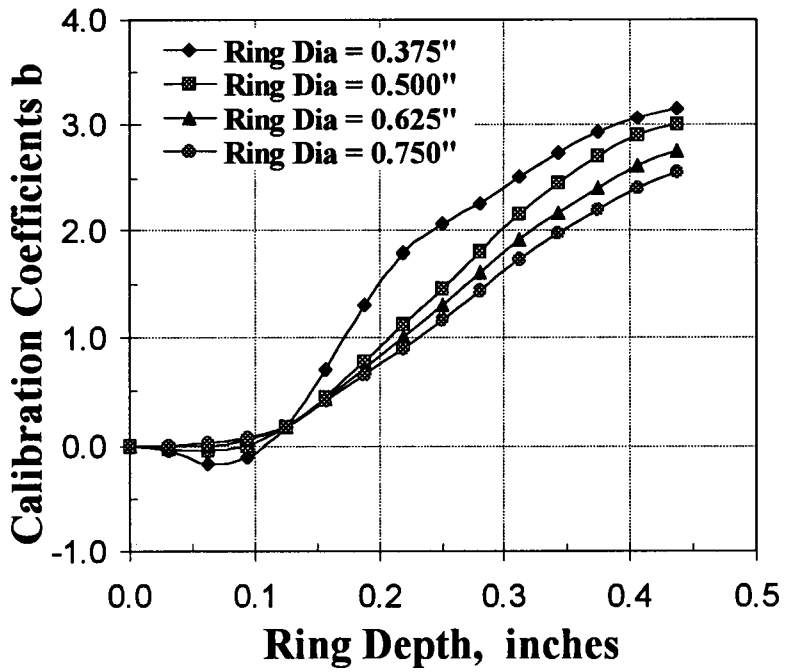

Figure 5.4. Effects of Ring Diameter on Coefficients $\bar{a}$ and $\bar{b}$.

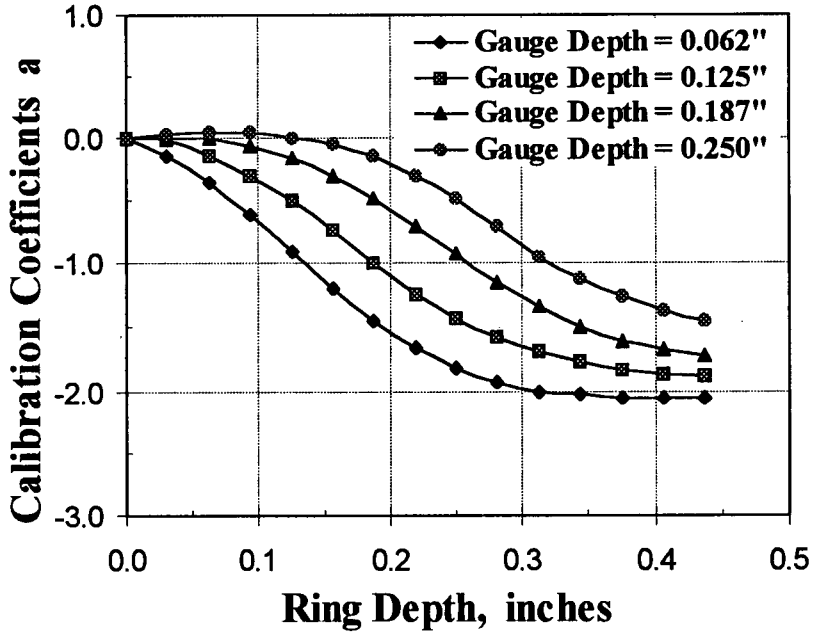

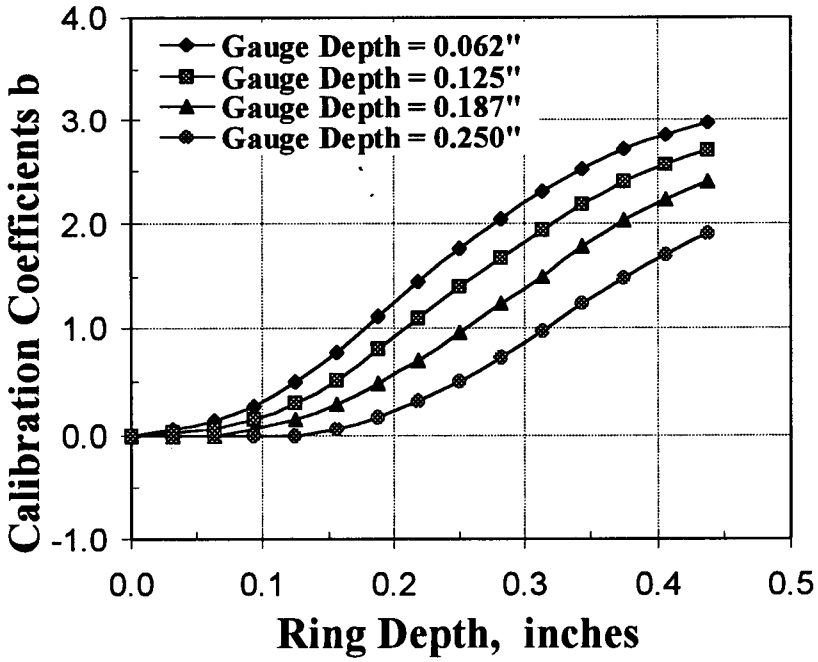

Figure 5.5 Effects of Strain Gauge Depth on Coefficients $\bar{a}$ and $\bar{b}$.

5.4 Ring-Hole Cutting Equipment

An end-mill device was designed and built to do the material cutting required for the ring-hole method. Figure 5.6 shows a photograph of the device and figure 5.7 shows a schematic cross-section. The device consists of an air-turbine driving a small end-mill. This air-turbine is mounted in an eccentric housing that can be rotated so that the turbine orbits around a circular path to mill the ring. The degree of eccentricity can be adjusted to change the radius of the ring.

Referring to Figure 5.7, the end-mill device consists of a high-speed air-turbine drive **1** mounted inside an eccentric cylinder **3** which in turn is mounted inside the inner micrometer **5** and secured by the hexagon bolt **2**. Vertical motion of the turbine is achieved by the relative rotation between inner micrometer **5** and outer micrometer **6**. The pusher **7** is used for tightening the micrometer thread to remove any "play" in the system. The pusher **7** is bolted together with the second worm gear **8** which is fixed with the housing of a four point contact ball bearing **9**. The bearing has a split inner ring to eliminate any looseness in the bearing. The worm gear and the upper part of the device are driven by the motor **10**. The entire device is mounted on the base fixture **12** and can be adjusted to the centre of the desired hole location by the adjustment bolts **11**.

Notice that figures 5.6 and 5.7 show different supporting units. The supporting unit shown in figure 5.6 is specifically designed to accommodate the test specimen used in this

study. The supporting legs shown in figure 5.7 are designed for general-purpose use. They have the advantage of having easily adjustable heights using the adjusting nuts **13**. The supporting legs can be adjusted to different heights when used on non-flat surfaces.

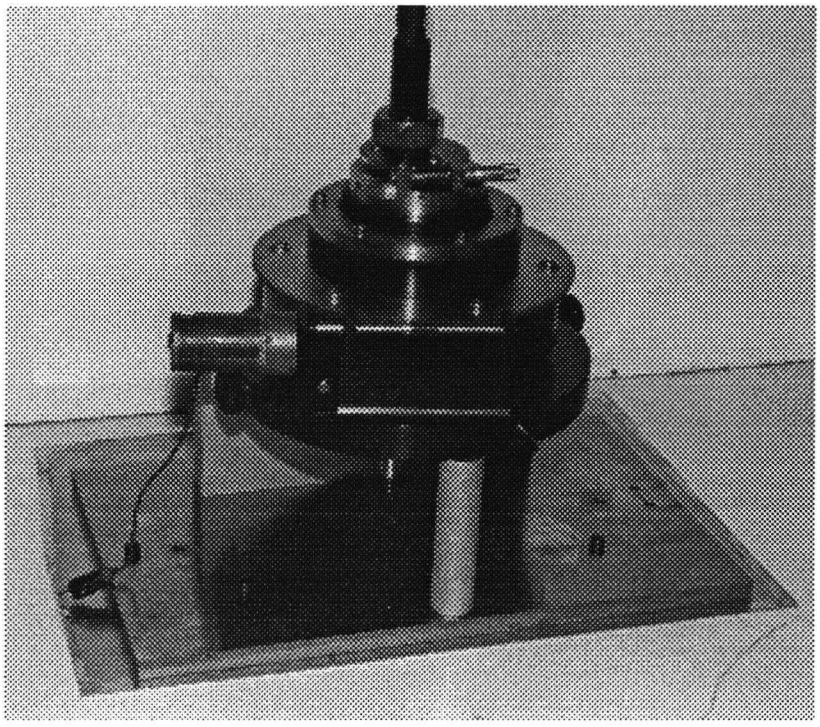

Figure 5.6 Photograph of the End-Milling Device.

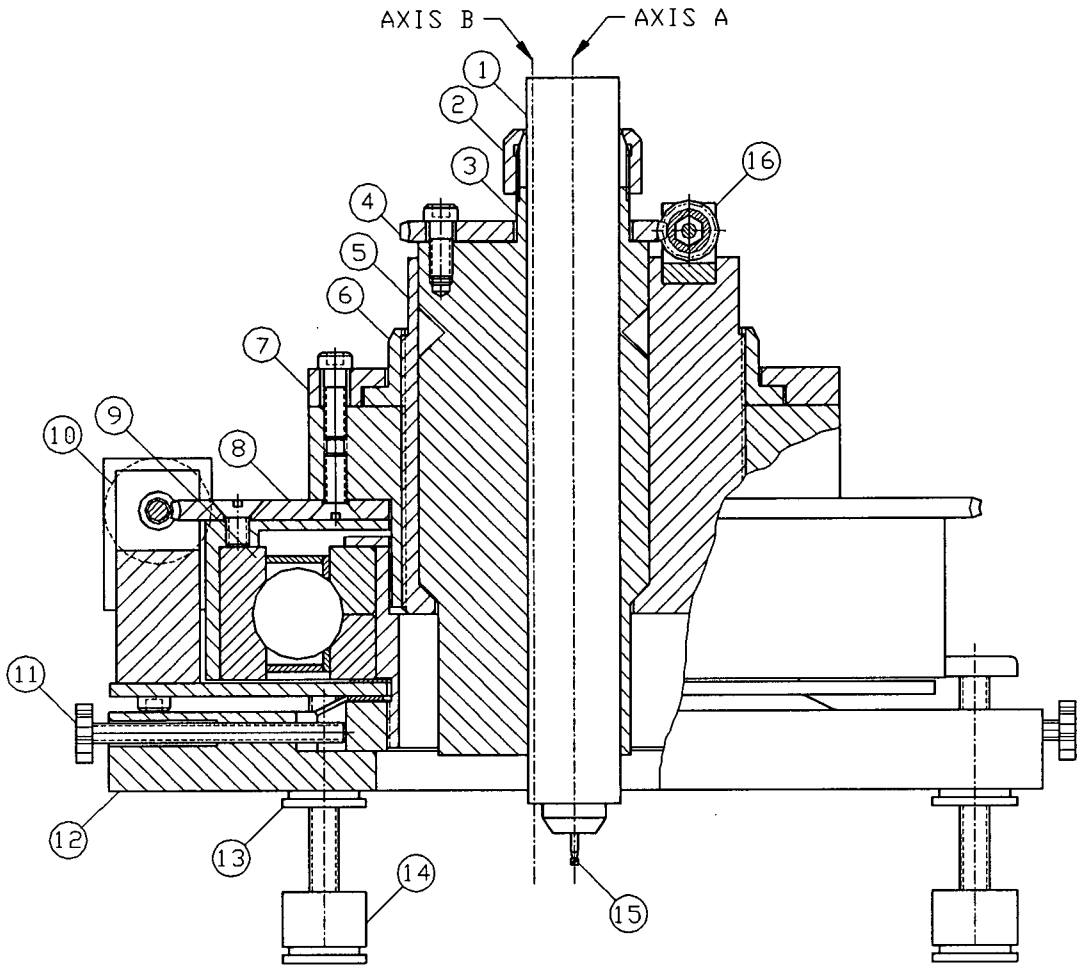

#	Item	#	Item
1	high Speed air turbine drive	9	four point contact ball bearing
2	hexagon bolt	10	motor
3	eccentric cylinder	11	adjusting bolt
4	worm gear 1	12	device base
5	inner micrometer	13	adjusting nuts
6	outer micrometer	14	supporting legs
7	pusher	15	milling cutter
8	worm gear 2	16	micrometer head

Figure 5.7 Cross-Section of the End-Milling Device.

A ring-hole drilling measurement starts by adjustment of the micrometer **5** so that the air turbine **1** together with the tip of the milling cutter **15** are centred relative to the centre of four point contact ball bearing **11** (axis A). The vertical height is adjusted so that the drill tip just touches the surface of the specimen. The height adjustment is achieved by rotating outer micrometer **6** while holding the inner micrometer **5** still. Drilling the hole proceeds by incrementally lowering the inner micrometer **5**, thereby causing the drill tip to move downward. The hole diameter adjustment is achieved by turning the micrometer head which drives the upper worm gear **4** so that the centre of the air turbine rotates around the centre of the eccentric cylinder (axis B).

After drilling the hole, a strip of 5 strain gauges, as shown in figure 5.8, is attached around the hole surface. This strip is half of a strip of ten strain gauges type 125MW made by Measurements Group, NC [35]. The hole diameter of 0.308 inches was chosen to match the 0.160 inches spacing of strain gauges so that when installed in the hole the gauges are equally spaced at 60° intervals around the centre hole. A specially designed jig was made to install the strain gauges. Figure 5.9 shows the cross-section of the jig.

The procedure for installing strain gauges by using the jig shown in figure 5.9 involves rolling the strain gauges around the rubber tube **3**, coating both the specimen and strain gauge with M-Bond 610 adhesive [36], inserting the jig and strain gauge into the centre hole of the specimen, curing the specimen and strain gauges at 125 ^{0}C in an oven for 6 hours.

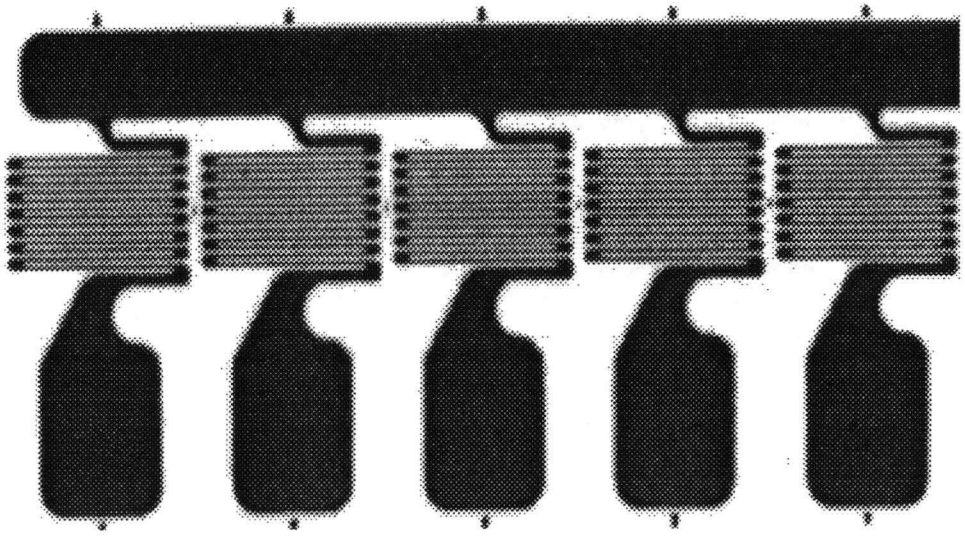

Figure 5.8 Strain Gauge Strip.

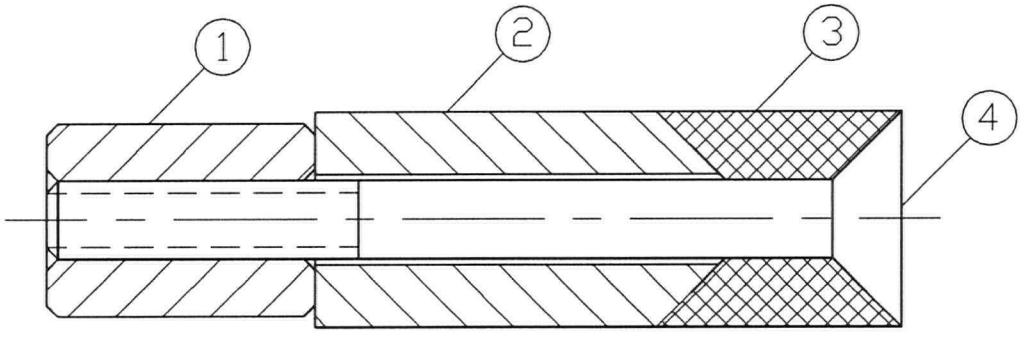

#	Item
1	adjusting nut
2	pusher
3	rubber tube
4	inserting bolt

Figure 5.9 Cross-Section of Strain Gauge Insertion Jig.

After attaching the strain gauges onto the surface of the centre hole, the annular ring is milled around the centre hole by the end-mill device. The milling procedure for the ring is similar to that for the hole. First, the upper micrometer head **16** is adjusted so that the end-mill tip is in position to cut the desired ring diameter. The vertical height is then adjusted by turning the micrometer **6** and holding the micrometer **5** still as for drilling the hole. Each increment is accurately measured by the inner and outer micrometer.

5.5 Experimental Verification

An experiment was conducted to verify the theoretical results from the finite element calculation shown in figures 5.4 and 5.5. The objectives of the experiments were:

1) to demonstrate the practicality of using ring-hole drilling for residual stress measurement.
2) to determine how well finite element calculations can predict the actual $\overline{a}$ and $\overline{b}$

A T6061 aluminum bar, with dimensions 4 x 2 x 13 inches, was used for the experiment. These dimensions were chosen so that the boundaries of the bar would be sufficiently distant from the ring-hole that the cutting would not significantly disturb the applied stresses. Figure 5.10 shows the arrangement of the specimen. The centre-hole was first drilled and the strain gauge strip was installed in it. Four additional single strain gauges were attached to the top and bottom surfaces of the sample to monitor the bending loads. The holes on each side were used to locate the specimen on the machine base to ensure repeatable positioning.

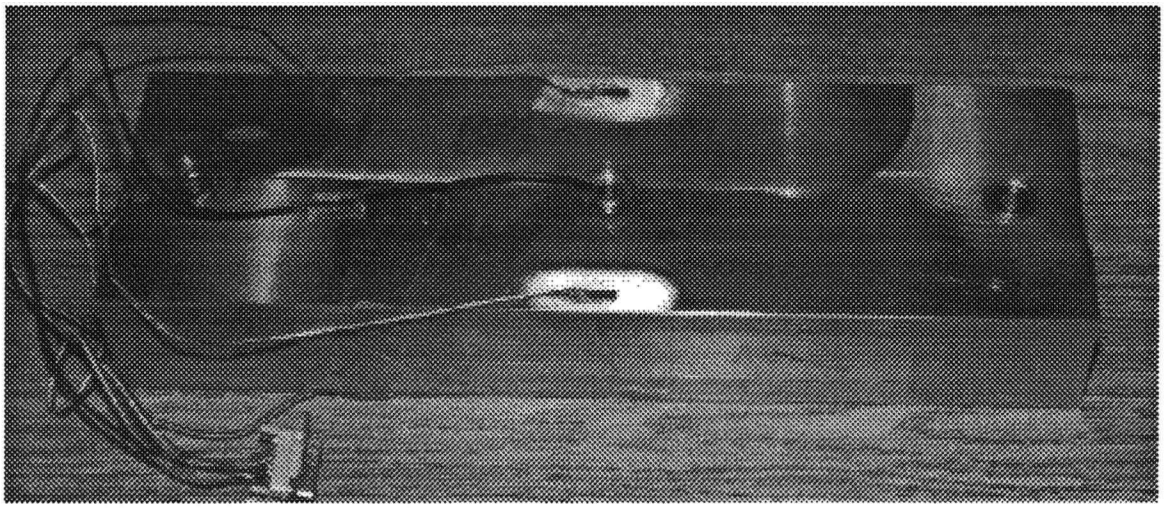

Figure 5.10 Photograph of the Ring-Hole Drilling Specimen.

The experiment was performed using the Tinius Olsen compression machine shown in figure 5.11. The specimen was subjected to a sequence of compressive loads from zero to 60,000 lbs., in 10,000 lbs. increments. Unwanted bending strains were monitored using the four additional strain gauges shown in figure 5.10. The specimen loading was adjusted by inserting shims at the ends of the specimen until the strains measured by the four strain gauges differed by less than 10%. The effects of the remaining bending strains were accounted for mathematically.

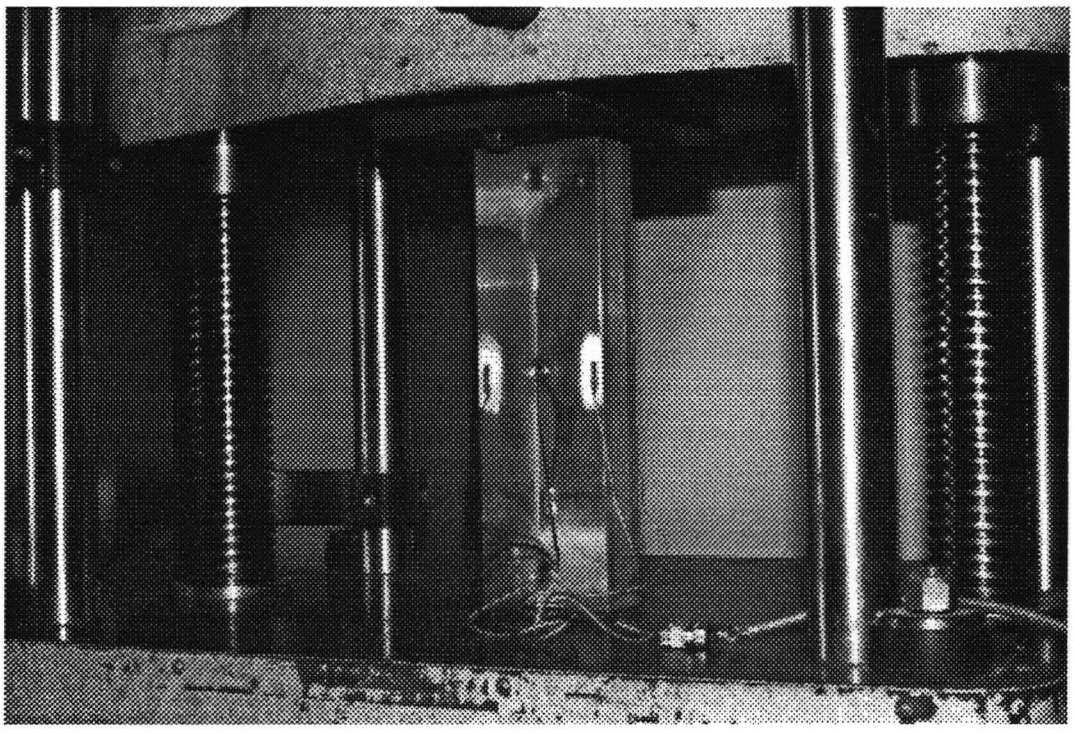

Figure 5.11 Specimen Loaded in a Tinius Olsen Compression Machine.

A centre hole was first drilled into the material. An annular ring was then milled successively in 22 depth increments, each increment being about 0.020 inches. Milling was done by the milling device shown in figures 5.6 and 5.7. After milling each increment, the specimen was subjected to a range of compressive loads from zero to 60,000 lbs, and the corresponding strains were recorded. The measured response of the strain gauges per unit load was determined from the gradient of the measured strain versus load. This procedure greatly reduces the effect of random strain measurement errors and eliminates the effect of any existing residual stresses in the material.

After milling the annular ring, the calibration coefficients $\bar{a}$ and $\bar{b}$ for a ring-hole drilling were calculated using the method described by Rendler and Vigness [15]. The results of the experiment are shown in figure 5.12. For comparison, the finite element results corresponding to the particular ring diameter and the strain gauge depth used in the experiment are also shown in the graph.

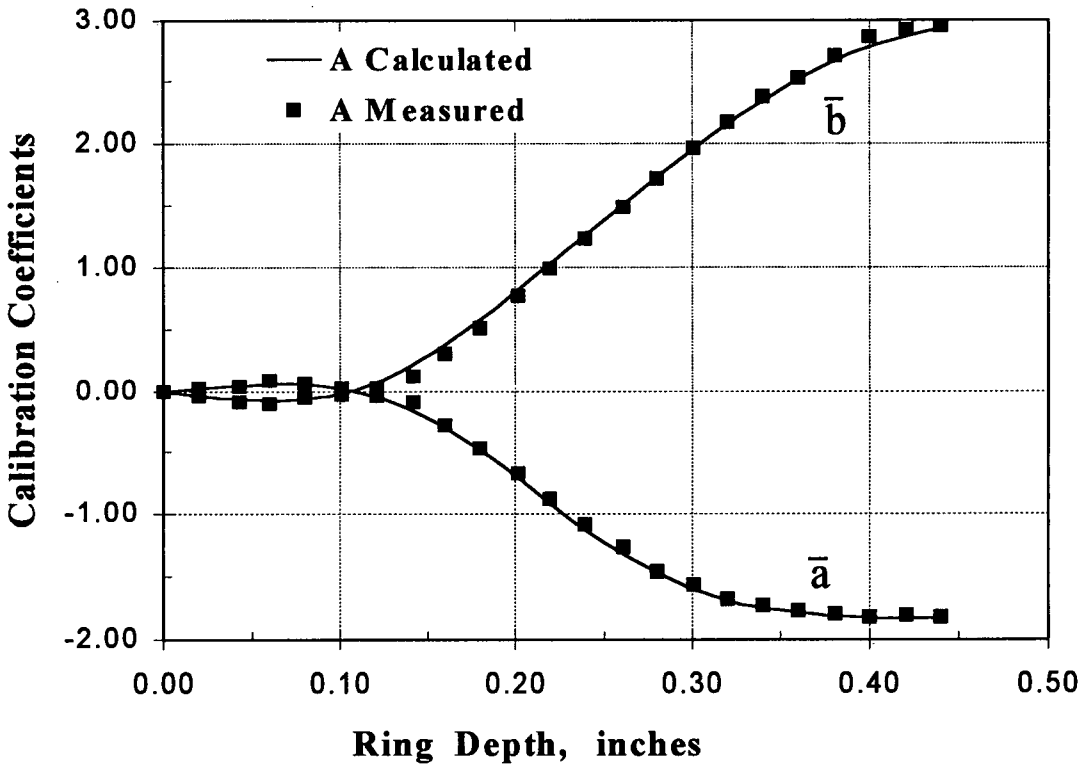

Figure 5.12 Comparison of the Experimentally Determined Calibration Coefficients with Theoretically Predicted Values.

The results in figure 5.12 show excellent agreement between the numerically calculated calibration coefficients and their values determined by experiment. The differences

between experimental results and theoretical predictions are typically less than 2%. The experimental results confirm that the theoretical prediction of the calibration coefficients of ring-hole are accurately applicable. In addition, the experimental work confirms ring-hole drilling using a milling device such as the one shown in figures 5.6 and 5.7 is a practical method for measuring residual stresses in a material.

5.6 Chapter Conclusion

This chapter introduced a new residual stress measurement method, Ring-Hole Drilling. By moving the strain gauges from the material surface to the interior, the proposed method overcomes the limitation of strain insensitivity to subsurface stresses of the hole-drilling and ring-core methods. The overall strain sensitivity of the ring-hole method is about double that of the ring-core method, and about four times that of the hole-drilling method. Experimental measurements made with the ring-hole method correspond very closely with theoretical expectations determined using the finite element method. The difference between the two results was typically less than 2%.

Like the existing methods, the theoretical approach of the ring-hole drilling is also based on the superposition of the stresses in the material. Finite element calculations show that the ring diameter, the ring depth and the strain gauge depth are the three important parameters affecting the calibration coefficients.

6. CONCLUSION

This thesis presents a study of methods for improving the accuracy and spatial resolution of residual stress measurements. This study has focused on two main approaches, improvement of the mathematical methods used for computing residual stresses from the measured strains, and improvement of the techniques used for making strain measurements that are more sensitive to the interior stresses. These investigations showed how the two approaches have significantly improved the accuracy of residual stress measurements by the layer-removal, hole-drilling and ring-core methods.

Two problems exist in the layer-removal method when calculations are based on solving Sachs' differential equations. Firstly, this approach is sensitive to strain measurement errors because of the differential terms. Secondly, equilibrium is not obeyed. The first part of this thesis demonstrated that these two problems are solved by using Linear Inverse Theory to obtain a stress solution.

The inverse solution method based on Linear Inverse Theory provides a more stable procedure for evaluating the residual stresses. To apply the method, Sachs' differential equation is reformulated into the form of an integral equation. This change avoids the problem of having to evaluate the strain derivatives. By applying the inverse method, stress equilibrium is easily enforced. The first part of this thesis describes the physics and governing

integral equations for typical layer removal methods. It then explains the application of the inverse solution method and compares different integral solution results.

To investigate the stability of the inverse solution, a set of synthetic data were generated and applied. Three functions, kernel functions, power series functions, and piecewise linear functions were chosen as the basis functions of the solution. Several important practical characteristics of the inverse solution were explored. Experimental data were also applied to the problem to demonstrate the practical use of the inverse method. The main findings from the investigations were:

1. When the strain data are "exact", the inverse solution method provides good stress results when used with kernel functions and piecewise linear functions. The piecewise linear functions are preferable since they produce relatively smooth curves. In contrast, the kernel functions generate unrealistic staircase shapes. However, both solutions obey stress equilibrium. The power series solution is numerically ill-conditioned and gives very unstable results.
2. In the presence of strain measurement errors, kernel functions produce the most stable results. Piecewise linear function solutions are more sensitive to strain data errors. However, equilibrium is always obeyed.
3. Smoothing can be introduced to the solution to reduce sensitivity to strain measurement errors. This is done by applying a deliberate data misfit. The size of the misfit and the resulting smoothing is chosen to give the statistically optimal balance between random

error reduction and preservation of the underlying solution. The results show that optimal smoothing effectively reduces the solution strain sensitivity for both kernel function and piecewise linear function solutions. For a kernel function solution, the steps of the staircase became more evenly spaced, while for linear function solutions the curves become smoother.

4. The stress results are distorted by the use of smoothing. The reduction of the effects of the strain measurement errors comes at the cost of a small overall distortion of the produced stresses. The reason is that the smoothing is achieved through a deliberate misfit between the given strain data and the produced stresses.

The second part of the thesis introduced a new residual stress measurement technique, ring-hole drilling. The new method combines aspects of both the hole-drilling and ring-core methods. It overcomes the interior stress resolution limitations of the previous two methods by moving strain gauges from the material surface to the centre hole. The results of the investigation show that by using ring-hole drilling, strain sensitivity can be improved significantly. The increased strain sensitivity reduces the effects of the strain measurement errors on the residual stress calculations.

The strain sensitivity is quantified through the calibration coefficients $\bar{a}$ and $\bar{b}$. Larger calibration coefficients result in higher strain sensitivity, and hence greater resistance to the effects of strain measurement errors. In this study, evaluation of $\bar{a}$ and $\bar{b}$ was first accomplished by the finite element method and then by experimental measurement. The finite

element results show that the ring diameter and the strain gauge depth are two important parameters affecting the value of the calibration coefficients.

In summary, the main contributions of the second part of the study for ring-hole drilling are:

1. The values of the calibration coefficients $\bar{a}$ and $\bar{b}$ are increased significantly compared with the ring-core method. The maximum value of $\bar{a}$ is increased from 0.54 to approximately 2, and the maximum value of $\bar{b}$ from 1.3 to approximately 3.5. The relative increase in calibration coefficients for the hole-drilling method is even larger. The hole-drilling calibration coefficients are only half of the corresponding ring-core values.
2. Finite element calculations are verified as an effective way of determining the values of the calibration coefficients $\bar{a}$ and $\bar{b}$ for the ring-hole drilling method. The experimental measurements showed that the differences between the finite element results and the experimentally determined values is typically less than 2%.
3. Ring-hole drilling is demonstrated as a practical method for measuring residual stresses in a material. The experimental procedure showed that ring-hole drilling can easily be achieved in practice by using a specially designed end-mill device.

In conclusion, the work presented in this thesis greatly improves the interior stress evaluation capabilities of layer removal, hole-drilling and ring-core methods. Through this

study, these commonly used destructive residual stresses measurement methods have become more accurate, more reliable and more practical to use.

REFERENCES

1. Dieter, G. E., Mechanical Metallurgy, Third Edition, McGraw-Hill, Toronto, 1986, pp.409-412.

2. Measurements Group, Inc. "Measurement of Residual Stresses by the Hole Drilling Strain-Gage Method." Tech Note TN-503-5, Measurements Group, Inc., Raleigh, NC, 1993, 20 pp.

3. François, M., et al., "X-Ray Diffraction Method." Chapter 5 in Handbook of Measurement of Residual Stresses, ed. Lu, J., Fairmot Press, Lilburn, GA, 1996, pp.71-131.

4. Holden, T. M., and Roy, G., "The Application of Neutron Diffraction to the Measurement of Residual Stress and Strain" Chapter 6, in Handbook of Measurement of Residual Stresses, ed. Lu, J., Fairmot Press, Lilburn, GA, 1996, pp.133-148.

5. Thompson, R. B., et al., "Ultrasonic Methods." Chapter 7 in Handbook of Measurement of Residual Stresses, ed. Lu, J., Fairmot Press, Lilburn, GA, 1996, pp.149-178.

6. Flavenot, J. F., "Layer Removal Method." Chapter 3 in Handbook of Measurement of Residual Stresses, ed. Lu, J., Fairmot Press, Lilburn, GA, 1996, pp.35-48.

7. Schajer, G. S., et al., "Hole-Drilling and Ring Core Methods." Chapter 2 in Handbook of Measurement of Residual Stresses, ed. Lu, J., Fairmot Press, Lilburn, GA, 1996, pp.5-34.

8. Sachs, G., "Evidence of Residual Stresses in Rods and Tubes." Zeitschrift für Metallkunde, Vol. 19, 1927, pp.352-259.

9. Lambert, J. W., "A Method of Deriving Residual Stress Equations." Proceedings SESA, Vol. 12, No. 1, May, 1953, pp.91-93.

10. Dodd, R. A., "Some Observations on the Determination of Residual Stresses in Cylindrical Metal Bodies by Sachs' Boring Method." Metallurgia, March, 1992, pp.109-114.

11. Hung, N. P., "The Use of an Automatic Data-Acquisition System for the Sachs' Residual Stress Measurement Method." Experimental Techniques, April, 1989, pp.24-26.

12. Mathar, J., "Determination of Initial Stresses by Measuring the Displacements Around Drilled Holes." Transactions ASME, Vol. 56, No. 2, 1934, pp.249-254.

13. Soete, W. and Vancrombrugge, R., "An Industrial Method for the Determination of Residual Stresses." Proceedings SESA, Vol. 8, No. 1, pp.17-28.

14. Kelsey, R. A., "Measuring Non-Uniform Residual Stresses by the Hole Drilling Method." Proceedings SESA, Vol. 14, No. 1, November, 1955, pp.181-194.

15. Rendler, N. J. and Vigness, I., "Hole-Drilling Strain-Gage Method of Measuring Residual Stresses." Experimental Mechanics, Vol. 6, No. 12, December, 1966, pp.577-586.

16. Bijak-Zochowski, M., "A Semidestructive Method of Measuring Residual Stresses." VDI-Berichte, Nr.312, 1978, pp.469-476.

17. Schajer, G. S., "Application of Finite Element Calculations to Residual Stress Measurements." Journal of Engineering Materials and Technology, Vol. 103, No. 2, April, 1981, pp.157-163.

18. Schajer, G. S., "Measurement of Non-Uniform Residual Stresses Using the Hole-Drilling Method." Journal of Engineering Material and Technology, Vol. 110, No. 4, October, 1988, Part I: pp.338-343, Part II: pp.344-349.

19. Milbradt, K. R., "Ring-Method Determination of Residual Stresses." Proceedings SESA, Vol. 9, No. 1, May, 1950, pp.63-74.

20. Gunnert, R., Method for Measuring Residual Stresses and its Application to a Study of Residual Welding Stresses. Almquist & Wiksell, Stockholm, 1955, 135pp.

21. Wolf, H. and Böhm "The Ring-Core Method for Measuring Residual Stresses and its Use with Turbines and Generator Shaft." Archive für Eisenhuttenwesen, Vol. 42, 1971, pp. 195-200.

22. Böhm, W., Stücker, E. and Wolf, H., "Principles and Potential Applications of the Ring-Core Method for Determining Residual Stress." Reports in Applied Measurement Vol. 4, No. 1, 1988, pp.5-20.

23. Oldenburg, D. W., "An Introduction to Linear Inverse Theory." IEEE Transactions on Geoscience and Remote Sensing, Vol. GE-22, No. 6, November, 1984, pp.665-674.

24. Menke, W., Geophysical Data Analysis: Discrete Inverse Theory, Academic Press, Toronto, 1984.

25. Parker, R. L., Geophysical Inverse Theory, Princeton University Press, New Jersey, 1994.

26. Press, W. H, et al., Numerical Recipes, Cambridge University Press, New York, 1987.

27. Liu, X., and Schajer, G. S, "More Reliable Calculations for Layer-Removal Residual Stress Measurements." Proceedings of SEM Spring Conference on Experimental Mechanics, June, 1997, pp.255-256.

28. American Society for Testing and Materials, "Standard Test Method for Determining Residual Stresses by the Hole-Drilling Strain Gage Method," ASTM Standard E837-95. 1995.

29. Schajer, G. S., "Use of Displacement Data to Calculate Strain Gauge Response in Non-Uniform Strain Fields." Strain, Vol. 29, No. 1, February, 1993, pp.9-13.

30. Tootoonian, M., Strain Sensitivity Enhancement for the Hole-Drilling Residual Stresses Measurement Method, M.A.Sc. Thesis, The University of British Columbia, Dec. 1993.

31. Keil, S., "Experimental Determination of Residual Stresses with the Ring-Core Method and an On-Line Measuring System," Experimental Techniques, Sept. 1992, pp.17-24.

32. Tootoonian, M., and Schajer, G. S., "Enhanced Sensitivity Residual-Stress Measurements Using Taper-Hole Drilling," Experimental Mechanics, Vol. 35, No. 2, January, 1995, pp.124-129.

33. Misra, A., and Peterson, H. A., "Examination of the Ring Method for Determination of Residual Stresses," Proceedings of SESA Spring Meeting, San Francisco, May, 1979, pp.268-272.

34. Timoshenko, S., and Goodier, J. M., Theory of Elasticity, Third Edition, McGraw-Hill, New York, 1970.

35. Measurements Group, Inc., Catalog 500, March, 1996, p.70.

36. Measurements Group, Inc., "Strain Gauge Application with M-Bond AE-10/15 and M-Bond GA-2 Adhesive Systems," Instruction Bulletin B-137-13, Measurements Group, Inc., Raleigh, NC, 1979, 4 pp.

APPENDIX

Layer-Removal Governing Equations

1. Circumferential Stress Derivation

Initially assume that the axial stresses are zero. When a bored-out section of radius r is removed from the cylinder, the stress contained in that bored-out section must be redistributed in a way such that force equilibrium is maintained. From thick-wall cylinder theory:

$$\sigma_\theta^{"}(R) = C + \frac{D}{R^2} \qquad \sigma_r^{"}(R) = C - \frac{D}{R^2} \qquad \text{A1}$$

where C and D are constants. The boundary conditions are:

$$\sigma_r^{"}(r) = -\sigma_r(r) \qquad \sigma_r^{"}(r_b) = 0$$

Application of these boundary conditions yields:

$$C = \frac{-\sigma_r(r)}{r^2 - r_b^2}\, r^2 \qquad D = \frac{-\sigma_r(r)}{r^2 - r_b^2}\, r^2\, r_b^2$$

Substitution of these results into equation A1 gives:

$$\sigma_\theta^{"}(R) = -\sigma_r(r)\frac{r^2}{R^2}\left(\frac{R^2 + r_b^2}{r^2 - r_b^2}\right) \qquad \sigma_r^{"}(R) = -\sigma_r(r)\frac{r^2}{R^2}\left(\frac{R^2 - r_b^2}{r^2 - r_b^2}\right) \qquad \text{A2}$$

From Hooke's law, the associated circumferential strain is:

$$E\,\varepsilon_\theta^{"}(r_b) = \sigma_\theta^{"}(r_b)$$

$$E\,\varepsilon_\theta^{"}(r_b) = -\sigma_r(r)\left(\frac{2r^2}{r^2 - r_b^2}\right) \qquad \text{A3}$$

The radial stress σ_r (R) and the circumferential stress σ_θ(R) must obey equilibrium. In polar co-ordinates, the equilibrium condition is:

$$\sigma_\theta(R) = \frac{d\left(R\sigma_r(R)\right)}{dR}$$

Integrating this equation and applying the condition $\sigma_r(r_b) = 0$ gives:

$$\int_r^{r_b} \sigma_\theta(R)\, dR = -r\sigma_r(r) \qquad \text{A4}$$

Equation A1 is then inverted to give σ_r(r) and substituted into equation A4. After rearranging, the relationship between the circumferential stress and the measured circumferential strain at the outer radius is:

$$E\varepsilon_\theta''(r_b) = \frac{2r}{r^2 - r_b^2} \int_r^{r_b} \sigma_\theta(R)\, dR \qquad \text{A5}$$

The axial strain due to a circumferential stress can be determined from generalized Hooke's law $E\varepsilon_a'' = -\nu\sigma_\theta''$:

$$E\varepsilon_a''(r_b) = \frac{-2\nu r}{r^2 - r_b^2} \int_r^{r_b} \sigma_\theta(R)\, dR \qquad \text{A6}$$

2. Axial Stress Derivation

Consider circumferential stresses are zero, the axial stress can be derived in the similar way from equilibrium. The relationship between axial stress and the axial strain is:

$$E\varepsilon_a''(r_b) = \frac{-2}{r_b^2 - r^2} \int_r^{r_b} \sigma_a(R)\, R\, dR \qquad \text{A7}$$

and the relationship between the axial stress and the circumferential strain is:

$$E\,\varepsilon_{\theta}^{"}(r_b) = \frac{2\nu}{r_b^2 - r^2} \int_r^{r_b} \sigma_a(R)\; R\; dR \qquad \text{A8}$$

3. Layer Removal Integral Equation

Consider both the axial stress and the circumferential stress exist at the same time, the measured strain results for the previous two cases can be added together since the system is linear elastic. The summation of equations A5 and A8 is:

$$\frac{E}{1-\nu^2}\left(\varepsilon_{\theta}^{"}(r_b) + \nu\varepsilon_{a}^{"}(r_b)\right) = \frac{-2r}{r_b^2 - r^2} \int_r^{r_b} \sigma_{\theta}(R)\; dR \qquad \text{A9}$$

and the summation of equations A6 and A7 is:

$$\frac{E}{1-\nu^2}\left(\varepsilon_{a}^{"}(r_b) + \nu\varepsilon_{\theta}^{"}(r_b)\right) = \frac{-2}{r_b^2 - r_2} \int_r^{r_b} \sigma_a(R)\; R\; dR \qquad \text{A10}$$

Grouping the constants:

$$\Psi(r) = \varepsilon_{\theta}^{"}(r_b) + \nu\varepsilon_{a}^{"}(r_b) \qquad\qquad \Lambda(r) = \varepsilon_{a}^{"}(r_b) + \nu\varepsilon_{\theta}^{"}(r_b)$$

Equation A9 and A10 become:

$$\frac{E}{1-\nu^2}\,\Psi(r) = \frac{-2r}{r_b^2 - r^2} \int_r^{r_b} \sigma_{\theta}(R)\; dR \qquad \text{A11}$$

$$\frac{E}{1-\nu^2}\,\Lambda(r) = \frac{-2}{r_b^2 - r_2} \int_r^{r_b} \sigma_a(R)\; R\; dR \qquad \text{A12}$$

4. Sachs' Differential Equations

Differentiate both sides with respect to r, the analytical solutions, termed Sachs' differential equations for circumferential and axial stresses are:

$$\sigma_\theta(r) = \frac{E}{1-\nu^2}\left(\frac{r_b^2 - r^2}{2r}\frac{d\Psi(r)}{dr} - \frac{r_b^2 + r^2}{2r^2}\Psi(r)\right) \qquad \text{A13}$$

$$\sigma_a(r) = \frac{E}{1-\nu^2}\left(\frac{r_b^2 - r^2}{2r}\frac{d\Lambda(r)}{dr} - \Lambda(r)\right) \qquad \text{A14}$$